**Article:**
Asael, D, Rouxel, O, Poulton, SW orcid.org/0000-0001-7621-189X et al. (2 more authors) (2018) Molybdenum record from black shales indicates oscillating atmospheric oxygen levels in the early Paleoproterozoic. American Journal of Science, 318 (3). pp. 275-299. ISSN 0002-9599

https://doi.org/10.2475/03.2018.01

# Molybdenum record from black shales indicates oscillating atmospheric oxygen levels in the early Paleoproterozoic

Dan Asael[1,2*], Olivier Rouxel[1$], Simon W. Poulton[3], Timothy W. Lyons[4], and Andrey Bekker[4]

[1] Department of Marine Geosciences, IFREMER, Centre de Brest, 29280 Plouzané, France

[2] Université de Brest, IUEM, UMR 6538, 29280 Plouzané, France

[3] School of Earth and Environment, University of Leeds, Leeds LS2 9JT, UK

[4] Department of Earth Sciences, University of California, Riverside, California, 92521, USA

Corresponding author: Dan Asael (dan.asael@yale.edu)

* present address: Yale University

$ present address: Department of Oceanography, University of Hawaii, Honolulu, HI 96822 USA

**ABSTRACT. The early Paleoproterozoic witnessed Earth's first major oxygenation, referred to as the Great Oxidation Event or GOE. The GOE began around 2.45 billion years ago (Ga) and progressed over hundreds of millions of years, as evidenced by multiple redox indicators, before coming to an abrupt end by ca. 2.06 Ga. The details of the GOE and the extent of oxygenation are still not resolved, however, and it is not clear how redox conditions across the GOE compare with those during the middle Proterozoic. In order to investigate the evolution of deep-ocean redox conditions during the GOE, we present Mo concentration and isotope data together with Fe speciation values for three key organic matter-rich shale units of the early Paleoproterozoic age (2.32 to 2.06 Ga). In addition, we present a new graphical representation of modeling suggesting that the oceanic Mo isotope system is highly sensitive to the balance between anoxic/suboxic and euxinic conditions until deep-ocean oxygenation, similar in scale to modern ocean oxygenation, is reached. Our approach indicates rising, yet oscillating atmospheric oxygen at 2.32 Ga, leading to an abrupt increase in Mo supply to the oceans and large Mo isotope variations under non-steady state conditions. The low seawater $\delta^{98}$Mo value based on the ca. 2.32 Ga black shales (0.32 ± 0.58‰) suggests that the oceans were still largely anoxic with locally developed euxinic conditions. Between 2.2 and 2.1 Ga, during the peak of the Lomagundi carbon isotope excursion, we observe higher $\delta^{98}Mo_{SW}$ values (1.23 ± 0.36‰) together with lower Mo concentrations in euxinic shales ([Mo] = 6.3 ± 9.0 ppm). We suggest that a decrease in the continental Mo input flux in the later part of the GOE was the main cause of this trend. Lower sulfide availability on the continents after protracted sulfide weathering associated with the early stages of the GOE, and efficient Mo removal in poorly oxygenated oceans under weakly euxinic conditions would both have contributed to the contraction of the Mo oceanic reservoir. By ca. 2.06 Ga, the Mo**

**isotope composition of seawater, as inferred from euxinic black shale intervals, became significantly lighter (0.70 ± 0.21‰), reflecting an increased rate of quantitative Mo removal due to the more widespread development of strongly euxinic conditions. Counterintuitively, seawater Mo concentrations recovered, likely due to an increase in the Mo input, which in turn might reflect enhanced weathering of organic carbon-rich shales deposited during the Lomagundi Event.**

## INTRODUCTION

It is now widely recognized that Earth experienced a major oxygenation event across the Archean-Proterozoic boundary, referred to as the Great Oxidation Event (GOE; Holland, 2002; Bekker, 2014a). Many lines of evidence support this interpretation (e.g., Farquhar and others, 2013; Lyons and others, 2014), including the development of extensive red beds (Cloud, 1968; Roscoe, 1969; Chandler, 1980) and the loss of detrital pyrite and uraninite from the sedimentary rock record (Roscoe, 1969). The absence of mass-independently fractionated (MIF) sulfur in sedimentary pyrite formed after 2.32 Ga (Bekker and others, 2004) provides a minimum age estimate for the Paleoproterozoic sulfur isotope transition, with atmospheric oxygen rising above 0.001% of present atmospheric levels (Pavlov and Kasting, 2002). Recent work has focused on clarifying the timing, magnitude and long-term effects of this oxygenation step by focusing on redox conditions shortly before (Anbar and others, 2007; Reinhard and others, 2013; Partin and others, 2013a), during (Bekker and Holland, 2012; Canfield and others, 2013; Kump and others, 2011; Partin and others, 2013b; Planavsky and others, 2012a; Scott and others, 2014; Gumsley and others, 2017) and after (Canfield, 1998; Planavsky and others, 2011) the GOE. The evolving picture of Earth's initial oxygenation now highlights a mildly, likely intermittently oxygenated atmosphere and locally oxygenated ocean surface prior to the GOE (Lyons and others, 2014; Olson and others, 2013), rigorous oxidative weathering of the continents and expansion of the marine sulfate reservoir across the GOE (Planavsky and others, 2012b), and a subsequent crash in surface redox conditions at ca. 2.06 Ga (Kump and others, 2011; Scott and others, 2014), prior to the short-lived return of iron formations and then development of widespread low-oxygen conditions by ca. 1.85 Ga (Poulton and others, 2010; Scott and others, 2008; Slack and Cannon, 2009; Kendall and others, 2011; Rasmussen and others, 2012).

Here we endeavor to further characterize early Paleoproterozoic redox conditions by combining Mo isotope analyses with Mo concentrations and Fe speciation data for black shales deposited between 2.32 and 2.06 Ga. We focus on three units, each representing a distinct time interval within the early Paleoproterozoic that were previously studied in detail using geochemical and sedimentological techniques to constrain the redox evolution of surface environments (Bekker and others, 2004; 2008; Rouxel and others, 2005; Scott and others, 2008; 2014; Partin and others, 2013a; b; Zerkle and others., 2017; Kipp and others, 2017). These units are the 2.32 Ga Rooihoogte / Timeball Hill formations (THF), the 2.2 to 2.1 Ga Sengoma Argillite Formation (SAF) of South Africa, and the 2.11 to 2.06 Ga Upper Zaogena Formation of Russia.

Our data provide a record of seawater redox conditions in the immediate aftermath of the Paleoproterozoic loss of sulfur MIF, during the peak of the Lomagundi Event (Bekker, 2014b), and immediately following the end of the Lomagundi Event. The primary focus of this study is the isotopic composition of Mo in early Paleoproterozoic seawater, which can provide insight into deep-ocean redox conditions. It has been demonstrated in modern environments that organic matter-rich sediments deposited under highly euxinic conditions (that is, an anoxic, sulfidic water column with >11 μM $H_2S$) have the potential to record the isotopic composition of contemporaneous seawater (Arnold and others, 2004; Asael and others, 2013; Barling and others, 2001; Dahl and others, 2011; Duan and others, 2010; Kendall and others, 2011, 2009; Neubert and others, 2008 ). It is important to note that under weakly euxinic conditions, removal of Mo to sediment may be non-quantitative, leading to a significant fractionation of up to 3‰ in the $^{98}Mo/^{95}Mo$ ratio, with the light isotopes concentrated in the sediment (Neubert and others, 2008; Nägler and others, 2011). Similarly, oxic and suboxic-anoxic (non-sulfidic) conditions are also characterized by large negative Mo isotope fractionations (Poulson and others, 2006; Poulson-Brucker and others, 2009). Hence, the isotopic composition of seawater

Mo reflects globally averaged Mo sinks and fluxes controlled by the redox state of the atmosphere-ocean system.

In order to differentiate between euxinic and non-euxinic conditions at the site of deposition we use the Fe speciation technique refined by Poulton and Canfield (2005), which has been employed in numerous Precambrian studies (for example, Asael and others, 2013; Kendall and others, 2011; Planavsky and others, 2011; Poulton and others, 2010; Reinhard and others, 2009; Scott and others, 2014; Thomson and others, 2015). The concentration of Mo in euxinic black shales is known to correlate positively with the concentration of Mo in seawater (Algeo and Lyons, 2006) and thus also provides important information on global sources and sinks of Mo and ocean redox state (Scott and others, 2008).

## GEOLOGICAL SETTING AND SAMPLE DESCRIPTION

The lower part of the THF was deposited in a deltaic setting of an open-marine basin (Coetzee and others, 2006) between the third and fourth Paleoproterozoic glacial events at ca. 2.32 Ga (Hannah and others, 2004). The unit consists of 200-m thick, upward-shallowing cycles, capped by a marine flooding surface, with organic matter-rich and pyritiferous deep-water, pro-delta shales grading upward into delta-front organic matter-lean shales and siltstones and, finally, shallow-water, delta-plain sandstones deposited above the fair-weather wave-base (Coetzee and others, 2006). The unit has experienced only lower-greenschist facies metamorphism. The lower part of the THF sets the minimum age of the GOE as defined by the loss of the S isotope MIF signal (Bekker and others, 2004). It is also the oldest known black shale unit that preserves large mass-dependent S isotope fractionations (MDF; Cameron, 1982; Bekker and others, 2004; Scott and others, 2014; Luo and others, 2016) and thus captures an important transition in Earth's redox state as related to global atmospheric and marine sulfur cycles.

The 2.2 to 2.1 Ga Sengoma Argillite Formation is comprised of up to 700 m of upward-shallowing organic matter-rich and pyritiferous shale, dolostone, chert, siltstone, and fine-grained sandstone that experienced lower-greenschist facies metamorphism. It was deposited in a deep, open-marine setting on the Kaapvaal craton, contemporaneous with the 2.2 to 2.1 Ga Lomagundi carbon isotope excursion (Bekker and others, 2008). The Lomagundi Event refers to a long-lasting positive carbon isotope excursion (with $\delta^{13}C$ values typically at, or even higher than, +8‰) preserved globally in sedimentary carbonates (Melezhik and Fallick, 1999). This excursion reflects globally enhanced burial of organic carbon, which could have generated over 20 times the amount of oxygen in the present atmospheric reservoir (Bekker and Holland, 2012 and references therein). Thus, the Lomagundi Event followed the Paleoproterozoic sulfur isotope transition (that is, the loss of MIF in sulfur isotopes) by 100 m.y. and likely represents a much larger increase in Earth's surface oxidation state.

The ca. 2.11 to 2.06 Ga Upper Zaogena Formation of the Ludikovian Series, Russian Karelia, consists of a 1500 m thick sequence of organic matter-rich shales and siltstones, cherts, subordinate dolostones, and basaltic tuffs. It was deposited in a marine basin in the aftermath of the Lomagundi Event (Melezhik and Fallick, 1999) when the marine sulfate reservoir apparently crashed (Scott and others, 2014), likely due to a large-scale de-oxygenation of the atmosphere and ocean. The formation experienced lower-greenschist facies metamorphism.

Since an important aspect of this study is to understand the unique behavior of Mo under euxinic conditions during the GOE and in its immediate aftermath by comparing geochemical data for these three units, all the samples selected for this study are lithologically similar, organic matter-rich shales. Furthermore, to limit variability in their depositional and diagenetic setting, we sampled only from thick stratigraphic intervals of homogenous, organic matter-rich shales.

## METHODOLOGY

Powdered samples were ashed in quartz beakers at 600°C for at least 24 h, and about 200 mg of each sample was dissolved in two steps using mixtures of $HNO_3$ + HF and $HNO_3$ + HCl acids. Solutions were then taken up with 20 mL of 7 mol/L HCl. Splits from each sample were taken, evaporated, and brought up in 5% $HNO_3$ for elemental analysis. Molybdenum concentrations were measured using a Thermo Scientific X-series 2 Quad ICP-MS, while Al and Fe concentrations were measured using a Horiba Jobin Yvon Ultima 2 ICP-AES at the Pôle Spectrométrie Océan (UMR 6538), Brest, France. Calibration of the instruments was performed by running a multi-element solution at different concentrations and blank solutions, while standardization was done via measurements of reference materials (BHVO-1, BHVO-2, SDO-1, Nod A-1, and Nod P-1). For the next step, the solutions were doped with Mo double spike and taken through a two-step chromatographic separation following the procedure of Asael and others (2013).

Molybdenum isotope measurements were performed using a Thermo Neptune MC-ICP-MS instrument at the Pôle Spectrométrie Océan (Ifremer), Brest, France. We used a $^{97}$Mo-$^{100}$Mo double-spike solution prepared gravimetrically from Oak Ridge Laboratory metal powders by Asael and others (2013). Optimization of the double-spike isotope composition relative to the SPEX in-house standard gave $^{95}$Mo/$^{98}$Mo, $^{97}$Mo/$^{98}$Mo, and $^{100}$Mo/$^{98}$Mo isotopic ratios of 0.278, 16.663, and 15.704, respectively. Data reduction was performed according to Siebert and others (2001), where iterations were repeated until the difference in the $\delta^{98}$Mo value between two consecutive iterations was smaller than 0.001‰. The typical number of iterations was $\leq$ 4. Within a given session, standards and samples were measured at a constant concentration. Selected geostandards were processed together with each set of columns resulting in the following values and external precision: Nod-P1 = -0.6 ± 0.10‰ (2SD, n=14); Nod-A1 = -0.44 ± 0.04‰ (2SD, n=11); and SDO-1 = 0.97 ± 0.08‰ (2SD, n=16). The typical

standard error of a single measurement (2SE) was 0.05‰. The MC-ICP-MS machine was operated in a low-resolution mode with an ESI Apex Q introduction system measuring all Mo isotope masses together with $^{91}Zr$ and $^{99}Ru$ in order to monitor isobaric interferences where correction was never necessary.

Molybdenum isotopic compositions are reported here using the conventional delta notation (in terms of $^{98}Mo/^{95}Mo$ ratios) relative to the NIST SRM 3134 with the value of +0.25‰ as suggested by Nägler and others (2014). During measurements we used the Mo SPEX standard (Lot 11-177Mo) as a lab standard, where calibration of the SPEX standard relative to NIST-3134 (lot 891307) and Rochester (Lot 802309E) gave:

$$\delta^{98/95}Mo_{SPEX} = \delta^{98/95}Mo_{NIST\text{-}3134} - 0.37 \pm 0.06‰ \text{ (2SD)}$$

$$\delta^{98/95}Mo_{SPEX} = \delta^{98/95}Mo_{Roch} - 0.05 \pm 0.06‰ \text{ (2SD)}$$

We used the following Fe speciation techniques in order to characterize the redox conditions of the depositional environment. The quantification of pyrite S was determined as described by Canfield and others (1986). Powdered samples were subjected to a hot chromous chloride leach for two hours in order to liberate pyrite S. Sulfide concentrations were determined either via iodometric titration, or gravimetrically following precipitation as $Ag_2S$, and converted to pyrite Fe concentrations using the stoichiometry of pyrite ($FeS_2$). Unsulfidized highly reactive Fe was quantified using the sequential extraction technique of Poulton and Canfield (2005), while reactive Fe was quantified via the boiling HCl leach of Berner (1970). Alternatively, we used the traditional approach to determine the degree-of-pyritization (DOP) parameter that was calibrated by Raiswell and others (1994). Highly reactive Fe refers to Fe, which is reactive towards sulfidation on early diagenetic timescales, while reactive Fe additionally includes poorly reactive silicate Fe (Canfield and others, 1992; Poulton and others, 2004), and these two Fe pools are used in the two different Fe-based redox proxies (see below).

For the sequential extraction, a separate sample split of approximately 100 mg was subjected to leaching by sodium acetate, sodium dithionite, and ammonium oxalate in order to quantify carbonate Fe (mostly siderite; $Fe_{carb}$), ferric oxide ($Fe_{ox}$), and magnetite ($Fe_{mag}$) pools, respectively. Quantification was accomplished using either an Agilent 5000 quadrupole ICP-MS or by atomic absorption spectroscopy, with a RSD of <5% for all stages. Reactive Fe was measured on a leachate derived from boiling approximately 100 mg of sample in concentrated HCl for sixty seconds, with the concentration determined spectrophotometrically. Total organic carbon (after removal of carbonate phases with dilute HCl) and total carbon were measured either on an Eltra C/S elemental analyzer or a Leco C/S elemental analyzer. Total inorganic carbon was calculated as the difference between total carbon and organic carbon.

A subset of 20 samples was analyzed by X-ray diffraction (XRD) to determine mineralogical composition using the Rietveld method, which yields semi-quantitative results. XRD analyses were conducted with a BRUKER AXS D8 Advance machine at IFREMER Institute, Brest, France.

## RESULTS

The mineralogical compositions determined for the studied sedimentary successions (table 1) are consistent with detrital sources (K-feldspar, plagioclase, quartz, forsterite, and muscovite) and low metamorphic grade as indicated by the presence of chlorite. XRD analyses also show the presence of authigenic minerals (fluorapatite and pyrite), minor oxidation of pyrite during drill-core storage (as indicated by the presence of rhomboclase, szomolnokite, jarosite, and gypsum), and localized hydrothermal alteration in the presence of low- to medium-temperature fluids (for example, pyrophyllite in the THF and, less so, SAF samples). Unreactive Fe mineral phases such as pyroxenes, amphiboles and garnets, which may represent higher metamorphic grade, are not found in our samples.

Our geochemical data are reported in table 2 and are also shown on depth profiles in figure 1. For the sequential Fe extraction we calculate the fraction of Fe considered to be highly reactive ($Fe_{HR}$) in the presence of dissolved sulfide (Canfield and others, 1992; Poulton and others, 2004) as $Fe_{HR} = Fe_{carb} + Fe_{ox} + Fe_{mag} + Fe_{py}$ (Poulton and Canfield, 2005). Following the criteria of Poulton and Canfield (2011), we identify water column euxinia where the ratio of highly reactive Fe to total Fe ($Fe_{HR}/Fe_T$) is > 0.38 and the ratio of sulfide Fe to highly reactive Fe ($Fe_{py}/Fe_{HR}$) is ≥ 0.7 (fig. 2) (Poulton and Canfield, 2011). The degree of pyritization was calculated as $DOP = Fe_{py}/(Fe_{py} + Fe_{HCl})$. Iron speciation data for SAF and UZF were partially reported in Scott and others, (20140).

Average Mo concentrations and Mo/TOC ratios (and total range) are as follows: for the THF, [Mo] = 19.7 ppm (4.34 to 67.7 ppm) and Mo/TOC = 12.5 (1.6 to 47.3); for the SAF, [Mo] = 6.3 ppm (1.35 to 36.6 ppm) and Mo/TOC = 0.6 (0.13 to 3.3); and for the UZF [Mo] = 25.2 ppm (1.6 to 180 ppm) and Mo/TOC = 2.1 (0.12 to 10.8).

Molybdenum isotope values range from -0.38 to +1.25‰ for the THF, from +0.00 to +2.21‰ for the SAF, and from +0.16 to +1.83‰ for the UZF. The samples that were clearly deposited from euxinic bottom waters (as suggested by the Fe-based redox proxies) give average ± 1SD values of $\delta^{98}Mo = +0.32 \pm 0.58$‰ for the THF, $\delta^{98}Mo = +1.23 \pm 0.36$‰ for the SAF, and $\delta^{98}Mo = +0.70 \pm 0.21$‰ for the UZF (fig. 3).

## DISCUSSION

### Molybdenum Modeling

In order to better understand the environmental changes potentially captured in the variability we observe in $\delta^{98}Mo$ values for euxinic samples, we use a simple mass-balance equation modified from Arnold and others (2004) to model the seawater Mo cycle, whereby:

$$f_{IN} \cdot \delta_{IN} = f_O \cdot \delta_O + f_S \cdot \delta_S + f_E \cdot \delta_E \quad \text{(eq. 1)}$$

Here, f represents the various fluxes into and out of the ocean, and δ is the isotopic composition of each flux term. The subscript 'IN' denotes the flux and isotopic composition of the combined riverine and hydrothermal inputs. As described in Asael and others (2013), the isotopic composition of the combined inputs is set at +0.5‰. This value is slightly lower than the average modern riverine input of 0.7‰ (Archer and Vance, 2008) as we include a hydrothermal input and consider that during long term continental weathering the value should be closer to the crustal average. The subscripts 'O', 'S', and 'E' denote oxic, anoxic/suboxic, and euxinic sinks, respectively. We use a fractionation factor of -3.0‰ for the oxic sink based on measurements of modern ferromanganese nodules and crusts (Barling and Anbar, 2004; Barling and others, 2001). Sediments from modern environments with anoxic (but not euxinic) and suboxic water columns have $\delta^{98}Mo$ compositions that range from -0.7 to +1.6‰ (Poulson and others, 2006). These environments represent a range of bottom-water redox conditions that allow for the recycling of Mn- and Fe-oxyhydroxides in the surface sediments with sulfate reduction restricted to pore waters (Scott and Lyons, 2012). For model purposes we use a fractionation factor of -1.0‰ as an average for Mo removal from seawater to the sediment under anoxic/suboxic conditions. We apply a fractionation factor of 0‰ for highly euxinic environments based on the isotopic composition of modern Black Sea sediments (Arnold and others, 2004). By setting the isotopic composition of the input at +0.5‰, we can design a three-component diagram that shows contours of $\delta^{98}Mo_{SW}$ values as a function of any given combination of sink fluxes (fig. 4a).

In addition to considering the burial fluxes to each of the three redox-defined settings required to produce the observed $\delta^{98}Mo_{SW}$ values, we can also explore their areal extent. To do so, we rewrite equation 1 as:

$$f_{IN} \cdot \delta_{IN} = A_O \cdot B_O \cdot \delta_O + A_S \cdot B_S \cdot \delta_S + A_E \cdot B_E \cdot \delta_E \quad \text{(eq. 2)}$$

where A is the relative areal extent (that is, fraction of the total seafloor) and B is the Mo burial rate of the oxic (O), anoxic/suboxic (S), and euxinic (E) sinks. Using published burial rates for each sink (Scott and others, 2008), we create a three-component diagram for areal extent (fig. 4b). From this exercise, we find that when $A_O$ is $\leq$ 98% of the seafloor (that is, $[A_E + A_S] \geq 2\%$ of ocean floor), $\delta^{98}Mo_{SW}$ is almost entirely controlled by the extent of the anoxic/suboxic sink because lines of constant $\delta^{98}Mo_{SW}$ closely follow lines with constant $A_E/A_S$ ratios in figure 4b. While the oxic sink results in a considerable fractionation from seawater, the burial rate in this setting (2 μg Mo/cm$^2$*10$^3$ yr) is two orders of magnitude lower than in anoxic/suboxic water column environments (250 μg Mo/cm$^2$*10$^3$ yr), where hydrogen sulfide is formed in pore waters (Scott and Lyons, 2012). At the other extreme, euxinic environments are very efficient at removing Mo from seawater with a burial rate of 1200 μg Mo/cm$^2$*10$^3$ yr. Because Mo removal in euxinic environments is close to 100% and, therefore, the net fractionation is essentially 0‰, it is the expansion and contraction of anoxic/suboxic settings alone that largely controls the $\delta^{98}Mo_{SW}$ values, unless the deep ocean is fully oxygenated, as it is today. An inset of the upper 5% of $A_o$ values (fig. 4c) shows that high $\delta^{98}Mo_{SW}$ values, similar to those found in the modern ocean ($\delta^{98}Mo_{SW} \approx 2.3$‰; Barling and others, 2001; Nägler and others, 2011) are only possible under input parameters used in this scenario in a fully oxygenated ocean when $A_O \geq 98\%$.

The burial rates from Scott and others, (2008) were calculated for the modern ocean. However, changes in the seawater Mo concentrations will change the burial rates of the

290 different redox environments in a proportional manner and therefore, will not effect our
291 calculations. For this reason we will use the term burial efficiency in our discussion to represent
292 potentially different absolute burial rate values that at the same time preserve constant ratios
293 between the redox settings.

294 The considerations above describe the Mo isotope system under ideal conditions.
295 However, the removal of Mo from the seawater to the sediments may deviate from ideal
296 conditions. Therefore, in the following we show a sensitivity test to this model by changing the
297 net fractionation factors associated with euxinic and anoxic/suboxic environments. First,
298 removal of Mo under euxinic conditions may not always be quantitative, which will result in
299 sediments with $\delta^{98}$Mo values lower than those of the contemporaneous seawater. This may
300 occur in euxinic settings when sulfide concentrations are below the critical threshold required
301 for complete conversion to sulfidized species (Tossell 2005). For example, net fractionations
302 of -0.5 ± 0.3‰ are found to occur in the Black Sea, Baltic Sea, and Cariaco Basin between
303 sediments and seawater (Arnold and others, 2004; Nägler and others, 2011; Neubert and others,
304 2008). Therefore, it might be more realistic to assign a net fractionation factor of -0.5‰ for the
305 removal of Mo in euxinic settings. In addition, in anoxic/suboxic environments where Mo is
306 mostly removed to the sediments through adsorption onto Fe-Mn oxyhydroxides, Mo can be
307 also incorporated into thiomolybdate species where sulfidic pore-waters develop.

308 In the case of low $H_2S$ levels, where $Fe_{py}/Fe_{HR}$ in the sediment is lower than the
309 euxinic threshold, the large fractionation associated with conversion of $MoO_4$ to $MoS_4$ (up to
310 6‰; Tossell, 2005) may be in action and would result in more negative $\delta^{98}$Mo values in the
311 sediment. Hence, under anoxic/suboxic conditions a net fractionation factor for Mo removal of
312 ca. -2‰ might be a more realistic value. A similar mechanism may work during Mo sorption
313 onto pyrite, where pyrite formation is an important process during diagenesis (Poulson-Brucker
314 and others, 2011). In figure 5 we show another set of three-component diagrams calculated

315 with the above-adjusted values for net fractionation factors in euxinic settings ($\Delta^{98}Mo_{SW\text{-}SED}$ =
316 0.5‰) and anoxic/suboxic settings ($\Delta^{98}Mo_{SW\text{-}SED}$ = 2.0‰). An important difference between
317 these two models is that while under the first set of values the maximum $\delta^{98}Mo_{SW}$ value without
318 a significant oxic sink is ca. +1.4‰, under the second set of adjusted values this ratio increases
319 to about +2.4‰ under the same redox conditions, which is similar to the modern seawater
320 value. Below we discuss geological conditions that could promote each of these two scenarios.

321 Iron Speciation

322 Iron speciation analysis is a common tool for paleoredox reconstructions based on black
323 shales and has been used extensively on Precambrian rocks as old as 2.7 Ga (Planavsky and
324 others, 2011; Reinhard and others, 2009). However, it has been demonstrated that during
325 diagenesis and low-grade metamorphism, unsulfidized, Fe-bearing highly reactive minerals
326 can be transformed to poorly reactive Fe-silicates, lowering $Fe_{HR}/Fe_T$ and increasing $Fe_{py}/Fe_{HR}$
327 ratios, although this process only tends to be significant when porewater sulfide concentrations
328 are very low (Poulton and others, 2010; Raiswell and others, 2011). Hence, a comparison
329 between the degree of pyritization (DOP) and $Fe_{py}/Fe_{HR}$ can help to address the potential for
330 alteration of primary geochemical signals (Cumming and others, 2013). Our data (fig. 6)
331 demonstrate a good correlation between DOP and $Fe_{py}/Fe_{HR}$. Based on this relationship, we are
332 confident that both of the Fe speciation methods represent a primary water column signal.
333 Furthermore, this relationship also demonstrates that poorly reactive Fe-silicates did not form
334 to a significant extent in the three studied units during diagenesis and metamorphism.

335 Iron speciation analysis of our Paleoproterozoic sample sets identifies both euxinic and
336 anoxic, non-sulfidic (that is, ferruginous) stratigraphic intervals in each of the three studied
337 units and, therefore, may have captured a record of Earth's fluctuating seawater redox
338 conditions from 2.32 Ga to 2.06 Ga. It is important to stress, however, that Fe speciation

analysis from a single drill-core only identifies local redox conditions for the time of deposition and cannot be extrapolated to global redox conditions without additional geochemical data (such as Mo isotope compositions) or a comprehensive study of many other correlative sections worldwide. As shown in figure 2, our THF samples, which were deposited immediately after the Paleoproterozoic loss of sulfur MIF (cf. Luo and others, 2016), record euxinic and non-euxinic conditions in approximately equal measure. Our SAF samples, which were deposited during the peak of the Lomagundi Event, show a primarily euxinic signal. Our UZF samples come from two drill cores. The stratigraphically lower core C-5190 (referred here as UZF-I) contains samples deposited under either ferruginous or oxic conditions. In contrast, core C-175 (referred here as UZF-II) primarily records euxinic water column conditions (fig. 2). Previously published pyrite sulfur isotope data from these two cores suggests that the UZF captured a crash in the seawater sulfate reservoir immediately following the end of the Lomagundi Event (Scott and others, 2014).

## Factors Controlling Molybdenum Enrichment

The three sedimentary units studied here show elevated Mo/Al ratios of 1.1 ± 0.6 ppm/wt% for the THF, 1.4 ± 2.2 ppm/wt% for the SAF, and 7.6 ± 11.6 ppm/wt% for the UZF, compared to an average of 0.19 ppm/wt% for upper continental crust (Taylor & McLennan, 1995). It should be noted that the THF has a high Al content (up to 12 wt%) relative to the upper continental crust (ca. 8 wt%), and thus the Mo/Al ratio likely underestimates the degree to which Mo was enriched from seawater. However, the Mo isotope composition of the three studied formations shows no correlation with Mo concentration or Mo/Al ratio (fig. 7), implying that the Mo in these rocks is predominantly authigenic and that the detrital Mo contribution was negligible. Considering the differences in Mo concentrations, both in the euxinic and non-euxinic samples, among these three units, it is clear that significant changes

363 in oceanic redox conditions, seawater composition, and/or the Mo input fluxes must have
364 occurred during this time interval.

365 The concentration of Mo and the ratio of Mo to total organic carbon (Mo/TOC) in euxinic
366 black shales have been shown to track the concentration of Mo in the overlying water column
367 (Algeo and Lyons, 2006). Furthermore, the concentration of Mo in seawater is thought to
368 reflect both the oxidative weathering flux from the continents and the extent of oxic, suboxic,
369 and euxinic oceanic settings due to differences in burial efficiencies in each of these
370 environments (Scott and others, 2008). Thus, it is important to consider Mo concentrations and
371 Mo/TOC ratios in concert with $\delta^{98}$Mo values. The average concentration of Mo in euxinic
372 samples from the THF, SAF, and UZF are 27.8 ± 26.9 ppm, 7.8 ± 10.14 ppm, and 31.6 ± 44.1
373 ppm, respectively. The Mo concentrations and Mo/TOC ratios show a similar trend with time,
374 with the lowest values observed in the SAF (fig. 3). The observed pattern of Mo concentrations
375 could also be a result of differences in sedimentation rates between the three units. However,
376 the uniform lithology, redox conditions (euxinic) and burial efficiency, together with the fact
377 that Mo/TOC ratios also show the same pattern between the three studied units, suggests that
378 different sedimentation rates were not an important factor. The co-variation between Mo
379 concentrations and TOC that is conspicuous in many Phanerozoic black shale units (Algeo and
380 Lyons, 2006), but also in the 2.5 Ga Mt. McRae shale (Anbar and others, 2007), is not observed
381 in our early Paleoproterozoic black shales (fig. 7c), suggesting secular variations in the Mo
382 seawater concentration.

383 Since Mo isotopes are most strongly fractionated in oxic environments where Mo burial
384 efficiencies are low, and Mo net isotope fractionations are smallest under euxinic conditions
385 where Mo burial efficiencies are highest, it is expected that for a given Mo input flux, low
386 $\delta^{98}Mo_{SW}$ values will correlate with low seawater Mo concentrations and therefore lower Mo
387 concentrations in black shales. Consistent with this argument, in fig. 4d we calculated

instantaneous, global oceanic Mo burial efficiencies in response to a change in the relative sizes of the different redox settings. By comparing fig. 4b and 4d one can see that an increase in the areal extent of euxinic environments would result in a decrease in the $\delta^{98}Mo_{SW}$ value and, at the same time, an increase in the average global burial efficiency. Consequently, once steady-state is re-established, lower [Mo] in seawater and in associated euxinic black shales will occur.

However, such a correlation is not observed in our dataset. For the SAF we observe $\delta^{98}$Mo values higher than those for both the THF and UZF, possibly reflecting the expansion of oxic and suboxic-anoxic environments at the expense of euxinic environments. Consistent with this interpretation, an increase in seawater sulfate content is inferred during the Lomagundi Event (Planavsky and others, 2012a; Scott and others, 2014). The expansion of oxic and suboxic-anoxic environments should have resulted in higher seawater Mo concentrations and higher Mo contents in euxinic shales of the SAF. In contrast, we observe low Mo concentrations in euxinic shales of the SAF. Conversely, euxinic shales of the UZF show low $\delta^{98}Mo_{SW}$ values, but higher Mo concentrations compared to the SAF. These observations suggest that other factors (in addition to ocean redox changes), such as variations in the Mo riverine flux and organic carbon burial on a local scale, as well as seawater sulfate content, could have influenced Mo isotope composition and concentration in Paleoproterozoic seawater. These issues will be discussed further in the next section.

## Molybdenum Isotope Variations and Inferred Seawater Values

To summarize, the Mo isotope composition of modern sediments deposited under euxinic conditions is known to approach or match that of seawater. For example, sediments from the euxinic Cariaco Basin and highly euxinic Black Sea have bulk isotopic compositions of +1.8‰ and +2.3‰, respectively, comparable to a seawater composition of +2.3‰ (Arnold and others, 2004; Nägler and others, 2011; Neubert and others, 2008). The isotopic composition of modern

seawater is significantly enriched relative to that of the average of the riverine and hydrothermal sources (+0.5‰; Asael and others, 2013), which is due to adsorption of the molybdate ion ($MoO_4^{2-}$) onto Mn- and Fe-oxyhydroxides under widespread oxic conditions in the modern ocean, a process that is associated with a fractionation factor of $\Delta^{98}Mo_{SW\text{-}OXIC} \approx$ 3‰ (Barling and Anbar, 2004; Barling and others, 2001; Goldberg and others, 2009). Thus, as the global extent of oxic and suboxic-anoxic conditions expands and contracts, the Mo isotope composition of seawater changes, and this signal may be captured in contemporaneous euxinic environments. Under globally euxinic conditions, where mechanisms for Mo removal are associated with smaller net fractionations, the isotopic composition of seawater will approach that of the riverine source. Based on these considerations, the Mo isotopic composition in euxinic black shales has been used to estimate the global redox state of the ancient oceans (Arnold and others, 2004; Asael and others, 2013; Dahl and others, 2011; Duan and others, 2010; Kendall and others, 2011; Lehmann and others, 2007). Kendall and others (2011) demonstrated that during the Paleoproterozoic the oceans were isotopically homogenous with respect to Mo. An estimate of the seawater $\delta^{98}$Mo value based on Paleoproterozoic sediments deposited in euxinic settings can therefore provide a paleoredox proxy for the global contemporaneous ocean.

It is important to note that even though the oceans were generally homogenous with respect to Mo, local, short-term fluctuations in Mo isotope composition of seawater may have still occurred at the sites of sedimentation. Such fluctuations could have resulted from Rayleigh distillation effects and local, non-quantitative Mo removal, which may drive the sediment Mo isotope composition in both directions (towards more negative values initially, but as the ambient seawater progressively shifted to a more positive composition sediments formed in contact with this evolved seawater would also record a positive shift). For this reason we chose

436 an average of the euxinic samples as the best estimate for the contemporaneous seawater Mo
437 isotope composition.

438 The THF dataset yields a seawater $\delta^{98}$Mo value of +0.32 ± 0.58‰ (1SD), which is
439 indistinguishable within uncertainty from the modern riverine flux, and suggests a limited
440 influence on $\delta^{98}Mo_{SW}$ value by adsorption and subsequent burial of Mo in association with Mn-
441 and Fe-oxyhydroxides in oxic and suboxic to anoxic deep-water settings. Critically, since Mo
442 burial efficiencies are low in oxic environments, oxic conditions could have been relatively
443 common at this time, but their influence over the seawater $\delta^{98}$Mo value was yet negligible. The
444 large range of Mo isotope values for euxinic samples from the THF of -0.34 to +1.25‰ implies
445 a dynamic Mo redox cycle and, possibly, a small seawater Mo reservoir. The S isotope
446 composition of pyrite in the THF indicates the presence of oxygen in the upper part of the
447 atmosphere, significant oxidative weathering of crustal sulfides, and a growing seawater sulfate
448 reservoir (Bekker and others, 2004; Scott and others, 2014). At the same time, Mo
449 concentrations and Mo/TOC ratios in the euxinic facies of the THF are larger than the average
450 Archean values for the same facies (typical Archean euxinic black shale Mo concentrations are
451 <5ppm; Scott and others, 2008). From these parameters, we infer a riverine Mo delivery to the
452 ocean under at least a moderately oxidizing atmosphere with a deep ocean still characterized
453 by widespread anoxia. It is plausible that massive weathering of continental sulfides in
454 association with the GOE (cf. Konhauser and others, 2011; Bekker and Holland, 2012)
455 enhanced sulfate delivery to the oceans and was an important mechanism for maintaining
456 widespread euxinic conditions on continental margins at this time, providing an efficient sink
457 for fluvially delivered Mo in relatively shallow-marine settings. The large variation in Mo
458 concentration and isotope composition observed even in euxinic black shales suggests varying
459 sulfide concentration in the water column, which resulted in episodic non-quantitative removal
460 of Mo to the sediments with low $\delta^{98}$Mo values, driving the seawater $\delta^{98}$Mo value to be more

positive, which in turn gave rise to more positive $\delta^{98}Mo$ values observed in the sediments of the THF.

During the peak of the Lomagundi Event, we estimate a $\delta^{98}Mo_{SW}$ value of +1.23 ± 0.36‰ (1STD), based on the average isotopic composition of euxinic intervals in the SAF and assuming no fractionation between authigenic Mo and coeval seawater. This represents a significant isotopic enrichment of seawater relative to the assumed combined fluxes with a Mo isotope composition of about +0.5‰ and also relative to the estimated $\delta^{98}Mo_{SW}$ value for the THF. In combination with previous discussion, this increase in the $\delta^{98}Mo_{SW}$ value clearly implies an expansion of suboxic-anoxic and, even oxic conditions.

Next, in the aftermath of the Lomagundi Event, the $\delta^{98}Mo_{SW}$ value decreased to +0.70 ± 0.21‰, based on the isotopic composition of euxinic shales from the UZF. The decreased seawater Mo isotope value relative to the SAF reflects a contraction of suboxic-anoxic and oxic depositional environments and an expansion of strongly euxinic settings. Our $\delta^{98}Mo_{SW}$ value for the UZF is largely in agreement with the previous estimate for the same unit by Asael and others (2013). At the same time, we also observe a recovery of the Mo concentrations in these black shales (relative to the SAF) to typical values for the Proterozoic (Scott and others, 2008).

In the previous section, we discussed why under ideal conditions and with an isotopically and quantitatively invariable Mo input flux an increase in the $\delta^{98}Mo_{SW}$ value is expected to be accompanied by an increase in Mo concentrations. However, in our data we see an opposite trend, in which the highest $\delta^{98}Mo_{SW}$ value is observed in the SAF where we also see the lowest Mo concentrations. This difference suggests that the Mo concentrations in our euxinic shales were not solely controlled by the relative size of the different Mo sinks as linked to ocean redox state. Low seawater Mo concentrations together with high $\delta^{98}Mo$ values may represent

484 enhanced trapping of Mo under weakly euxinic conditions where Mo is not quantitatively
485 removed and isotopically fractionated.

486 In order to further test this hypothesis, we adjusted the fractionation factors as discussed
487 above (that is, mildly euxinic conditions and non-quantitative Mo removal in euxinic settings
488 where removal of Mo is very efficient) to account for a higher $\delta^{98}Mo_{SW}$ value associated with
489 a larger global Mo burial efficiency. The adjusted fractionation factors may partially account
490 for the observed trends (fig. 5). Taking into account the high relative burial rate of organic
491 carbon during the Lomagundi Event, it is plausible that high organic carbon loading across the
492 oceans led to weakly euxinic conditions in a largely anoxic-ferruginous ocean. Under these
493 conditions and in combination with locally developed nutrient limitation oscillating redox
494 conditions would be common in the oceans. In contrast to situations when euxinia develops in
495 silled basins, we infer that on continental margins relatively high burial rates of organic carbon
496 accompanied by anoxia and euxinia would limit extensive and persistent accumulation of high
497 levels of $H_2S$ in the water column.

498 The pattern of the Mo concentrations in the three units might also reflect changes in the
499 Mo riverine input flux. The high Mo concentrations observed in the THF likely reflect
500 substantial continental sulfide weathering due to the rapid rise in atmospheric oxygen level in
501 association with the GOE. The SAF was deposited more than 150 Ma after this initial pulse of
502 sulfide weathering products when sulfide availability on the continents, and, as a result, the Mo
503 riverine input decreased (Bachan and Kump, 2015). The UZF samples show an increase in Mo
504 concentrations, possibly due to widespread recycling of Mo-enriched sediments (such as the
505 organic matter-rich shales deposited during the GOE), which may have occurred for the first
506 time in Earth's history (cf. Bekker and Holland, 2012 and Kump and others, 2011). It should
507 be noted that even though the SAF sediments show low Mo concentrations (average [Mo] =
508 6.3 ± 9.0 ppm), these values are still well above that of average continental crust ([Mo] ≈ 1ppm

for continental crust; Taylor and McLennan (1995)), and therefore weathering of these sediments can contribute substantially to the recovery of Mo in seawater.

As discussed above, our modelling indicates that the balance between suboxic-anoxic and fully euxinic sinks controlled much of the Mo inventory and its isotope composition, at least until the deep ocean became oxygenated in the Phanerozoic. Plotted on the model figures, the $\delta^{98}Mo_{SW}$ values from the THF, UZF, and SAF sections (shaded areas on fig. 4b and fig. 5b) represent slightly different $A_E/A_S$ ratios, but hold very little information regarding the extent of oxic conditions. There is independent evidence for the growth of the seawater sulfate reservoir during the GOE (in the time between deposition of the THF and SAF; Bekker and Holland, 2012; Bekker and others, 2004; Planavsky and others, 2012a; Scott and others, 2014), reflecting low rates of pyrite burial under more oxygenated seawater conditions, and high organic carbon loading into sediments during the Lomagundi Event, resulting in significant oxygen release to surface environments. Considering the above, it is most parsimonious to infer that the extent of euxinic conditions during deposition of the SAF was limited by the expansion of oxic shallow-water and suboxic-anoxic deep-water conditions. We therefore propose that the observed pattern of Mo isotope values and concentrations indicates that before and during deposition of the THF (ca. 2.32 Ga), the oceans were largely anoxic with locally developed euxinic areas. By ca. 2.15 Ga when the SAF was deposited, strongly euxinic conditions became rare at the expanse of widespread weakly euxinic settings in which removal of Mo to the sediments in pore waters was non-quantitative. By ca. 2.06 Ga when the UZF was deposited, the oceans switched to a new state with anoxic-suboxic deep-waters and locally developed strongly euxinic conditions in upwelling zones and intracratonic basins.

It is also reasonable to assume that after the Lomagundi Event, the isotopic composition of the Mo input to the ocean was more positive because of exposure and weathering of black shales with higher $\delta^{98}Mo$ values on the continents. In this case the shift between the seawater

value and the input becomes smaller, implying an even smaller extent of Mo-fractionating environments (that is suboxic-anoxic and oxic settings). For example, if we use a value of 0.7‰ (closer to the average modern fluvial input; Archer and Vance 2008) for the average post-GOE Mo input instead of 0.5‰, $\delta^{98}$Mo contour lines on Fig. 4 will shift by 0.2‰ up and seawater values would reflect a larger extent of euxinia. For the UZF, this would imply a greater fall in seawater oxygen level right after the Lomagundi Event.

The $\delta^{98}Mo_{SW}$ values for the later part of the Proterozoic (fig. 3) range between +1.0 and +1.2‰ (Kendall and others, 2011; 2009; Dahl and others, 2011). In contrast, the $\delta^{98}Mo_{SW}$ value for the 2.5 Ga 'whiff' event (+1.39 ± 0.22‰; Duan and others, 2010), when atmospheric oxygen most likely did not reach the levels expected for the Lomagundi Event, is nevertheless similar to our value for the SAF, consistent with the Mo isotope composition of seawater across the GOE being largely decoupled from atmospheric oxygen level and rather reflecting the extent of suboxic-anoxic settings. Scott and others (2014) made a similar argument for S isotope composition of seawater by comparing pyrite S isotope systematics during and after the Lomagundi Event. Together, these observations suggest a strong coupling between the S and Mo cycles in the Paleoproterozoic.

## CONCLUSIONS

The Mo isotope composition of early Paleoproterozoic black shales provides evidence for dramatic changes in the redox state and composition of the global ocean in the aftermath of the pervasively anoxic Archean. During the early stage of the GOE, at ca. 2.32 Ga, we observe a dynamic oceanic Mo cycle, likely caused by highly variable atmospheric oxygen levels and an enhanced Mo riverine flux into the ocean at a time when massive weathering of continental sulfides occurred for the first time in Earth's history. The studied organic matter-rich shales

record large variations in Mo isotope composition, which were likely produced under variable sulfide concentrations in the water column.

At ca. 2.15 Ga, in the middle of the Lomagundi Event, atmospheric oxygen levels stabilized, seawater sulfate concentrations peaked, extensive burial of organic matter occurred, and seawater Mo concentrations decreased. The oceans were largely anoxic with extensively developed, weakly euxinic conditions beneath oxic surface waters. In the immediate aftermath of the Lomagundi Event, we observe the lowest known $\delta^{98}Mo_{SW}$ values after the GOE, supporting previous evidence for a crash in atmospheric and oceanic oxygen levels. Recycling of the organic matter-rich sediments deposited during the Lomagundi Event likely took place, enhancing the Mo supply to the oceans with supracrustal values. Euxinic conditions during this interval were likely limited to intracratonic basins and zones of upwelling on continental margins, where high level of hydrogen sulfide accumulated, whereas the deep ocean remained in a low redox state for the following billion years of Earth's history.

ACKNOWLEDGEMENTS

We thank E. Ponzevera, Y. Germain, S. Cheron, A. Boissier, and Steve Bates for technical assistance. This work was supported by IFREMER and funding from Labex Mer (ANR-10-LABX-19-01), NSF (#0820676) and Europole Mer. A.B. acknowledges support from NSF grant EAR-05-45484, NASA Astrobiology Institute Award NNA04CC09A, and an NSERC Discovery and Accelerator Grants. P. Medvedev from the Institute of Geology, Karelian Research Center, Russia is thanked for arranging access to the UZF samples. The NASA Exobiology and Astrobiology programs provided funds to TWL.

## Figure captions

Figure 1. Chemostratigraphy of the studied units: (a) THF; (b) SAF; (c) UZF-II; and (d) UZF-I. For each sample values of $Fe_{HR}/Fe_T$, $Fe_{py}/Fe_{HR}$, Mo concentrations, Mo/TOC, and $\delta^{98}Mo$ are plotted against their stratigraphic position (stratigraphic columns are modified from Zerkle and others, 2017; Bekker and others, 2008; and Scott and others, 2014, respectively). Dashed lines in the Fe speciation plots represent the threshold values for euxinia of $Fe_{HR}/Fe_T > 0.38$ and $Fe_{py}/Fe_{HR} > 0.7$. Filled symbols correspond to the upper axis ($Fe_{HR}/Fe_T$, [Mo], and $\delta^{98}Mo$) and open symbols to the lower axis ($Fe_{py}/Fe_{HR}$ and Mo/TOC). GCB is the Great Chert Breccia that unconformably underlies the Rooihoogte and Timeball Hill formations.

Figure 2. Iron speciation data for the studied units presented as $Fe_{HR}/Fe_T$ vs. $Fe_{py}/Fe_{HR}$. A euxinic criteria of $Fe_{HR}/Fe_T > 0.38$ and $Fe_{py}/Fe_{HR} > 0.7$ as suggested by Poulton and Canfield (2011) was used. Note that euxinic samples are found in each of the studied units.

Figure 3. a, b, and c show $\delta^{98}Mo$, [Mo], and Mo/TOC values through time, symbols with dots represent euxinic samples. (d) $\delta^{98}Mo_{SW}$ estimates from Late Archean and Proterozoic units (squares denote published data from: Asael and others, 2013 (2.05 Ga); Canfield and others, 2013 (2.08 Ga); Duan and others, 2010 (2.5 Ga); Kendall and others, 2011 (1.85 Ga), 2009 (1.36 Ga); Dahl and others, 2011 (0.75 Ga); and Lehmann and others, 2007 (0.54 Ga), whereas circles denote data from this study. Error bars represent 1standard deviation of the samples used to calculate the contemporaneous seawater $\delta^{98}Mo$ value, $\delta^{13}C_{sw}$ curve from Planavsky and others, 2014 is in the background.

Figure 4. Three-component diagrams of the Mo seawater isotope system: (a) showing relative fluxes of Mo to redox-different sinks where $f_O$, $f_E$, and $f_s$ represent the Mo fluxes to oxic, euxinic, and suboxic-anoxic sinks, respectively; (b) showing relative seafloor area of the redox-different sinks, where $A_O$, $A_E$, and $A_s$ represent areas of oxic, euxinic, and suboxic-anoxic ocean floor, respectively (based on the average burial rates given in Scott and others (2008)); (c) an inset of the upper 5% of (b), demonstrating that high $\delta^{98}Mo_{SW}$ values, such as those found in the modern ocean, can only be achieved if the ocean floor is dominated by oxic environments ($A_O > 98\%$); and (d) showing instantaneous, global oceanic Mo burial efficiency in response to a change in the relative sizes of the different redox settings (based on the burial rates given in Scott and others (2008)). The dotted grey, dark-grey, and pale-grey areas represent the $\delta^{98}Mo_{SW}$ values of the THF, SAF, and UZF, respectively.

Figure 5. Three-component diagrams of the Mo seawater isotope system with the adjusted fractionation factors ($\Delta^{98}Mo_{SW\text{-}SED}$ = 0.5‰ in euxinic settings and $\Delta^{98}Mo_{SW\text{-}SED}$ = 2.0‰ in suboxic-anoxic settings) as discussed in the text: (a) showing relative fluxes of Mo to redox-different sinks where $f_O$, $f_E$, and $f_s$ represent Mo fluxes to oxic, euxinic, and anoxic-suboxic sinks, respectively; (b) showing relative seafloor area of the redox-different sinks, where $A_O$, $A_E$, and $A_s$ represent areas of oxic, euxinic, and anoxic-suboxic ocean floor, respectively (based on the burial rates given in Scott and others (2008)); and (c) showing instantaneous, global oceanic Mo burial efficiency in response to a change in the relative sizes of the different redox settings (based on the burial rates given in Scott and others (2008)). The dark-grey area represents the $\delta^{98}Mo_{SW}$ values of the SAF.

Figure 6. Correlation between degree of pyritization (DOP) and $Fe_{py}/Fe_{HR}$ values for our samples. The solid line represent linear regression where the two dashed lines the 95% confidence level. The good correlation observed between DOP and $Fe_{py}/Fe_{HR}$ suggest that both of the Fe speciation methods represent a primary water column signal and that poorly reactive

629 Fe-silicates did not form to a significant extent in the three studied units during diagenesis and
630 metamorphism.

631

632 Figure 7. Molybdenum isotope compositions vs. Mo concentrations (a), 1/[Mo] (b),
633 Mo/Al ratios (c), and Mo concentrations vs. TOC content (d). Dotted symbols represent euxinic
634 samples. Co-variation is not apparent for any of the units on these four plots. The strong co-
635 variation between [Mo] and TOC content, commonly observed for Phanerozoic black shales
636 (e.g., Algeo and Lyons, 2006), is also not apparent in our early Paleoproterozoic data.

637

638 **References**


639 1. Algeo, T.J., Lyons, T.W., 2006. Mo-total organic carbon covariation in modern anoxic marine
640 environments: Implications for analysis of paleoredox and paleohydrographic conditions.
641 Paleoceanography 21, 1–23. doi:10.1029/2004PA001112
642 2. Anbar, A.D., Duan, Y., Lyons, T.W., Arnold, G.L., Kendall, B., Creaser, R. a, Kaufman, A.J.,
643 Gordon, G.W., Scott, C.T., Garvin, J., Buick, R., 2007. A whiff of oxygen before the great
644 oxidation event? Science 317, 1903–6. doi:10.1126/science.1140325
645 3. Archer, C., Vance, D., 2008. The isotopic signature of the global riverine molybdenum flux
646 and anoxia in the ancient oceans. Nature Geosci., 1(9), 597–600. doi:10.1038/ngeo282
647 4. Arnold, G.L., Anbar, A.D., Barling, J., Lyons, T.W., 2004. Molybdenum isotope evidence for
648 widespread anoxia in mid-Proterozoic oceans. Science 304, 87–90.
649 doi:10.1126/science.1091785
650 5. Asael, D., Tissot, F.L.H., Reinhard, C.T., Rouxel, O.J., Dauphas, N., Lyons, T.W., Ponzevera,
651 E., Liorzou, C., Chéron, S., 2013. Coupled molybdenum, iron and uranium stable isotopes as
652 oceanic paleoredox proxies during the Paleoproterozoic Shunga Event. Chem. Geol. 362, 193–
653 210.
654 6. Bachan, A., & Kump, L. R., 2015. The rise of oxygen and siderite oxidation during the
655 Lomagundi Event. PNAS, 112(21), 6562–6567. http://doi.org/10.1073/pnas.1422319112
656 7. Barling, J., Anbar, A.D., 2004. Molybdenum isotope fractionation during adsorption by
657 manganese oxides. Earth Planet. Sci. Lett. 217, 315–329. doi:10.1016/S0012-821X(03)00608-
658 3
659 8. Barling, J., Arnold, G.L., Anbar, A.D., 2001. Natural mass-dependent variations in the isotopic
660 composition of molybdenum. Earth Planet. Sci. Lett. 193, 447–457. doi:10.1016/S0012-
661 821X(01)00514-3
662 9. Bekker, A., 2014a. Great Oxygenation Event, In: Encyclopedia of Astrobiology, Springer-
663 Verlag, p. 1-9.

664 10. Bekker, A., 2014b, Lomagundi Carbon Isotope Excursion, In: Encyclopedia of Astrobiology,
665 Springer-Verlag, p. 1-6.
666 11. Bekker, A., Holland, H.D., 2012. Oxygen overshoot and recovery during the early
667 Paleoproterozoic. Earth Planet. Sci. Lett. 317-318, 295–304. doi:10.1016/j.epsl.2011.12.012
668 12. Bekker, A., Holland, H.D., Wang, P.-L., Rumble, D., Stein, H.J., Hannah, J.L., Coetzee, L.L.,
669 Beukes, N.J., 2004. Dating the rise of atmospheric oxygen. Nature 427, 117–20.
670 doi:10.1038/nature02260
671 13. Bekker, A., Holmden, C., Beukes, N.J., Kenig, F., Eglinton, B., Patterson, W.P., 2008.
672 Fractionation between inorganic and organic carbon during the Lomagundi (2.22–2.1 Ga)
673 carbon isotope excursion. Earth Planet. Sci. Lett. 271, 278–291. doi:10.1016/j.epsl.2008.04.021
674 14. Berner, R. A., 1970. Sedimentary Pyrite Formation. American Journal of Science. 268, 1-23.
675 15. Cameron, E. M., 1982. Sulphate and sulphate reduction in early Precambrian oceans. Nature,
676 296, 145–148. doi.org/10.1038/296145a0
677 16. Canfield, D.E., 1998. A new model for Proterozoic ocean chemistry. Nature 396, 450–453.
678 17. Canfield, D.E., Ngombi-Pemba, L., Hammarlund, E.U., Bengtson, S., Chaussidon, M.,
679 Gauthier-Lafaye, F., Meunier, A., Riboulleau, A., Rollion-Bard, C., Rouxel, O.J., Asael, D.,
680 Pierson-Wickmann, A.-C., El Albani, A., 2013. Oxygen dynamics in the aftermath of the Great
681 Oxidation of Earth's atmosphere. Proc. Natl. Acad. Sci. U.S.A. 110, 16736–41.
682 doi:10.1073/pnas.1315570110
683 18. Canfield, D.E., Raiswell, R., Bottrell, S., 1992. The reactivity of sedimentary iron minerals
684 toward sulfide. Am. J. Sci. 292, 659–683.
685 19. Canfield, D.E. DE, Raiswell, R., Westrich, J.J.T., Reaves, C.M., Berner, R. a., 1986. The use
686 of chromium reduction in the analysis of reduced inorganic sulfur in sediments and shales.
687 Chem. Geol. 54, 149–155. doi:10.1016/0009-2541(86)90078-1
688 20. Chandler, F.W., 1980. Proterozoic redbed sequences of Canada. Canadian Geological Survey
689 Bulletin 311, 53.

690 21. Cloud, P.E., 1968. Atmospheric and Hydrospheric Evolution on the Primitive Earth: Both
691 secular accretion and biological and geochemical processes have affected earth's volatile
692 envelope. Science 160, 729–736. doi:10.1126/science.160.3829.729
693 22. Coetzee, L. L., Beukes, N. J., Gutzmer, J., & Kakegawa, T., 2006. Links of organic carbon
694 cycling and burial to depositional depth gradients and establishment of a snowball Earth at
695 2.3Ga. Evidence from the Timeball Hill Formation, Transvaal Supergroup, South Africa. South
696 African Journal Of Geology, 109(1-2), 109–122. doi:10.2113/gssajg.109.1-2.109
697 23. Cumming, V. M., Poulton, S. W., Rooney, A. D., & Selby, D. (2013). Anoxia in the terrestrial
698 environment during the late Mesoproterozoic. Geology, 41(5), 583–586.
699 http://doi.org/10.1130/G34299.1
700 24. Dahl, T.W., Canfield, D.E., Rosing, M.T., Frei, R.E., Gordon, G.W., Knoll, Aclintsuggest.H.,
701 Anbar, A.D., 2011. Molybdenum evidence for expansive sulfidic water masses in ~750Ma
702 oceans. Earth Planet. Sci. Lett. 311, 264–274. doi:10.1016/j.epsl.2011.09.016
703 25. Duan, Y., Anbar, A.D., Arnold, G.L., Lyons, T.W., Gordon, G.W., Kendall, B., 2010.
704 Molybdenum isotope evidence for mild environmental oxygenation before the Great Oxidation
705 Event. Geochim. Cosmochim. Acta 74, 6655–6668. doi:10.1016/j.gca.2010.08.035
706 26. Farquhar, J., Zerkle, A.L., Bekker, A., 2013. Geological and Geochemical Constraints on
707 Earth's Early Atmosphere, Treatise of Geochemistry, Elsevier, v. 6, p. 91-138.
708 27. Goldberg, T., Archer, C., Vance, D., Poulton, S.W., 2009. Mo isotope fractionation during
709 adsorption to Fe (oxyhydr)oxides. Geochim. Cosmochim. Acta 73, 6502–6516.
710 doi:10.1016/j.gca.2009.08.004
711 28. Gumsley, A.P., Chamberlain, K.R., Bleeker, W., Söderlund, U., de Kock, M.O., Larsson, E.R.,
712 and Bekker, A., 2017. Timing and tempo of the Great Oxidation Event, Proc. Natl. Acad. Sci.
713 U.S.A. 114, 1811-1816.
714 29. Hannah, J. L., Bekker, A., Stein, H. J., Markey, R. J., & Holland, H. D., 2004. Primitive Os and
715 2316 Ma age for marine shale: Implications for Paleoproterozoic glacial events and the rise of
716 atmospheric oxygen. . Earth Planet. Sci. Lett. 225, 43–52. doi:10.1016/j.epsl.2004.06.013

30. Holland, H.D., 2002. Volcanic gases, black smokers, and the Great Oxidation Event. Geochim. Cosmochim. Acta 66, 3811-3826.
31. Kendall, B., Creaser, R. a., Gordon, G.W., Anbar, A.D., 2009. Re–Os and Mo isotope systematics of black shales from the Middle Proterozoic Velkerri and Wollogorang Formations, McArthur Basin, northern Australia. Geochim. Cosmochim. Acta 73, 2534–2558. doi:10.1016/j.gca.2009.02.013
32. Kendall, B., Gordon, G.W., Poulton, S.W., Anbar, A.D., 2011. Molybdenum isotope constraints on the extent of late Paleoproterozoic ocean euxinia. Earth Planet. Sci. Lett. 307, 450–460. doi:10.1016/j.epsl.2011.05.019
33. Kipp, M.A., Stüeken, E.E., Bekker, A., Buick, R., 2017. Selenium isotopes record extensive marine suboxia during the Great Oxidation Event, Proc. Natl. Acad. Sci. U.S.A. 114, 875-880.
34. Konhauser, K.O., Lalonde, S.V., Planavsky, N.J., Pecoits, E., Lyons, T.W., Mojzsis, S.J., Rouxel, O.J., Barley, M.E., Rosìere, C., Fralick, P.W., Kump, L.R., Bekker, A., 2011. Aerobic Pyrite Oxidation and Acid Rock Drainage During the Great Oxidation Event, Nature 478, 369-373.
35. Kump, L.R., Junium, C., Arthur, M. a, Brasier, A., Fallick, A., Melezhik, V., Lepland, A., Crne, A.E., Luo, G., 2011. Isotopic evidence for massive oxidation of organic matter following the great oxidation event. Science 334, 1694–1696. doi:10.1126/science.1213999
36. Lehmann, B., Nägler, T.F., Holland, H.D., Wille, M., Mao, J., Pan, J., Ma, D., Dulski, P., 2007. Highly metalliferous carbonaceous shale and Early Cambrian seawater. Geology 35, 403. doi:10.1130/G23543A.1
37. Luo, G., Ono, S., Beukes, N. J., Wang, D. T., Xie, S., & Summons, R. E., 2016. Rapid oxygenation of Earth's atmosphere 2.33 billion years ago. Sci. Advan. 2, 1–9. doi.org/10.1126/sciadv.1600134
38. Lyons, T.W., Reinhard, C.T., Planavsky, N.J., 2014. The rise of oxygen in Earth's early ocean and atmosphere. Nature 506, 307–15. doi:10.1038/nature13068

743 39. Melezhik, V., Fallick, A., 1999. Extreme 13Ccarb enrichment in ca. 2.0 Ga magnesite–
744 stromatolite-dolomite–"red beds" association in a global context: a case for the world-wide
745 signal enhanced by a local environment. Earth-Sci. Rev. 48, 71–120.
746 40. Nägler, T. F., Anbar, A. D., Archer, C., Goldberg, T., Gwyneth, G. W., Greber, N. D., Siebert,
747 C., Sohrin, Y., and Vance, D. 2014. Proposal for an International Molybdenum Isotope
748 Measurement Standard and Data Representation. Geostandards and Geoanalytical Research 38,
749 149–151.
750 41. Nägler, T.F., Neubert, N., Böttcher, M.E., Dellwig, O., Schnetger, B., 2011. Molybdenum
751 isotope fractionation in pelagic euxinia: Evidence from the modern Black and Baltic Seas.
752 Chem. Geol. 289, 1–11. doi:10.1016/j.chemgeo.2011.07.001
753 42. Neubert, N., Nägler, T.F., Böttcher, M.E., 2008. Sulfidity controls molybdenum isotope
754 fractionation into euxinic sediments: Evidence from the modern Black Sea. Geology 36, 775.
755 doi:10.1130/G24959A.1
756 43. Olson, S. L., Kump, L. R., & Kasting, J. F. (2013). Quantifying the areal extent and dissolved
757 oxygen concentrations of Archean oxygen oases. Chemical Geology, 362, 35–43.
758 http://doi.org/10.1016/j.chemgeo.2013.08.012
759 44. Partin, C.A., Bekker, A., Planavsky, N.J., Scott, C.T., Gill, B.C., Li, C., Podkovyrov, V.,
760 Maslov, A., Konhauser, K.O., Lalonde, S.V., Love, G.D., Poulton, S.W., Lyons, T.W., 2013a.
761 Large-scale fluctuations in Precambrian atmospheric and oceanic oxygen levels from the record
762 of U in shales. Earth Planet. Sci. Lett. 369-370, 284–293. doi:10.1016/j.epsl.2013.03.031
763 45. Partin, C.A., Lalonde, S. V., Planavsky, N. J., Bekker, A., Rouxel, O. J., Lyons, T. W.,
764 Konhauser, K. O., 2013b. Uranium in iron formations and the rise of atmospheric oxygen.
765 Chemical Geology, 362, 82–90. http://doi.org/10.1016/j.chemgeo.2013.09.005
766 46. Pavlov, A.A., Kasting, J.F., 2002. Mass-independent fractionation of sulfur isotopes in Archean
767 sediments: strong evidence for an anoxic Archean atmosphere. Astrobio. 2, 27–41.
768 doi:10.1089/153110702753621321

769 47. Planavsky, N.J., McGoldrick, P., Scott, C.T., Li, C., Reinhard, C.T., Kelly, A.E., Chu, X.,
770 Bekker, A., Love, G.D., Lyons, T.W., 2011. Widespread iron-rich conditions in the mid-
771 Proterozoic ocean. Nature 477, 448–51. doi:10.1038/nature10327
772 48. Planavsky, N.J., Bekker, A., Hofmann, A., Owens, J.D., Lyons, T.W., 2012a. Sulfur record of
773 rising and falling marine oxygen and sulfate levels during the Lomagundi event. Proc. Natl.
774 Acad. Sci. U.S.A. 109, 18300–18305. doi:10.1073/pnas.1120387109
775 49. Planavsky, N.J., Rouxel, O.J., Bekker, A., Hofmann, A., Little, C.T.S., Lyons, T.W., 2012b.
776 Iron isotope composition of some Archean and Proterozoic iron formations. Geochim.
777 Cosmochim. Acta 80, 158–169. doi:10.1016/j.gca.2011.12.001
778 50. Planavsky, N., Partin, C., Bekker, A., 2014. Carbon Isotopes as a Geochemical Tracer, In:
779 Encyclopedia of Astrobiology, Springer-Verlag, p. 1-6.
780 51. Poulson, R.L., Siebert, C., McManus, J., Berelson, W.M., 2006. Authigenic molybdenum
781 isotope signatures in marine sediments. Geology 34, 617. doi:10.1130/G22485.1
782 52. Poulson-Brucker, R., McManus, J., Severmann, S., Owens, J., Lyons, T. W., 2011. Trace metal
783 enrichments in Lake Tanganyika sediments: Controls on trace metal burial in lacustrine
784 systems. Geoch. Cosmochim. Acta, 75, 483–499. doi:10.1016/j.gca.2010.09.041
785 53. Poulson Brucker, R. L., McManus, J., Severmann, S., & Berelson, W. M., 2009. Molybdenum
786 behavior during early diagenesis: Insights from Mo isotopes. Geochem. Geophys. Geosyst.,
787 10(6), Q06010. http://doi.org/2009 10.1029/2008GC002180
788 54. Poulton, S.W., Canfield, D.E., 2005. Development of a sequential extraction procedure for iron:
789 implications for iron partitioning in continentally derived particulates. Chem. Geol. 214, 209–
790 221. doi:10.1016/j.chemgeo.2004.09.003
791 55. Poulton, S.W., Canfield, D.E., 2011. Ferruginous Conditions: A Dominant Feature of the Ocean
792 through Earth's History. Elements 7, 107–112. doi:10.2113/gselements.7.2.107
793 56. Poulton, S.W., Fralick, P.W., Canfield, D.E., 2010. Spatial variability in oceanic redox structure
794 1.8 billion years ago. Nat. Geosci. 3, 486–490. doi:10.1038/ngeo889

795 57. Poulton, S.W., Krom, M.D., Raiswell, R., 2004. A revised scheme for the reactivity of iron
796 (oxyhydr)oxide minerals towards dissolved sulfide. Geochim. Cosmochim. Acta 68, 3703–
797 3715. doi:10.1016/j.gca.2004.03.012
798 58. Raiswell, R., Canfield, D. E., Berner, R. A., 1994. A comparison of iron extraction methods for
799 the determination of degree of pyritisation and the recognition of iron-limited pyrite formation.
800 Chem. Geol. 111, 101–110. doi:10.1016/0009-2541(94)90084-1
801 59. Raiswell, R., Reinhard, C. T., Derkowski, A., Owens, J., Bottrell, S. H., Anbar, A. D., Lyons,
802 T. W., 2011. Formation of syngenetic and early diagenetic iron minerals in the late Archean
803 Mt. McRae Shale, Hamersley Basin, Australia: New insights on the patterns, controls and
804 paleoenvironmental implications of authigenic mineral formation. Geochim. Cosmochim.
805 Acta, 75, 1072–1087. doi:10.1016/j.gca.2010.11.013
806 60. Rasmussen, B., Fletcher, I.R., Bekker, A., Muhling, J.R., Gregory, C.J., Thorne, A.M., 2012.
807 Deposition of 1.88-billion-year-old iron formations as a consequence of rapid crustal growth.
808 Nature 484, 498–501. doi:10.1038/nature11021
809 61. Reinhard, C.T., Planavsky, N.J., Lyons, T.W., 2013. Long-term sedimentary recycling of rare
810 sulphur isotope anomalies. Nature 497, 100–103. doi:10.1038/nature12021
811 62. Reinhard, C.T., Raiswell, R., Scott, C., Anbar, A.D., Lyons, T.W., 2009. A late Archean
812 sulfidic sea stimulated by early oxidative weathering of the continents. Science 326, 713–6.
813 doi:10.1126/science.1176711
814 63. Roscoe, S.M., 1969. Huronian rocks and uraniferous conglomerates in the Canadian Shield.
815 Geol. Surv. Canada.
816 64. Rouxel, O.J., Bekker, A., Edwards, K.J., 2005. Iron isotope constraints on the Archean and
817 Paleoproterozoic ocean redox state. Science 307, 1088–91. doi:10.1126/science.1105692
818 65. Scott, C., Lyons, T.W., 2012. Contrasting molybdenum cycling and isotopic properties in
819 euxinic versus non-euxinic sediments and sedimentary rocks: Refining the paleoproxies. Chem.
820 Geol. 324-325, 19–27. doi:10.1016/j.chemgeo.2012.05.012

66. Scott, C.T., Lyons, T.W., Bekker, A., Shen, Y., Poulton, S.W., Chu, X., Anbar, A.D., 2008. Tracing the stepwise oxygenation of the Proterozoic ocean. Nature 452, 456–9. doi:10.1038/nature06811

67. Scott, C., Wing, B.A., Bekker, A., Planavsky, N.J., Medvedev, P., Bates, S.M., Yun, M., Lyons, T.W., 2014. Pyrite multiple-sulfur isotope evidence for rapid expansion and contraction of the early Paleoproterozoic seawater sulfate reservoir. Earth Planet. Sci. Lett. 389, 95–104. doi:10.1016/j.epsl.2013.12.010

68. Siebert, C., Nägler, T.F.T., Kramers, J.J.D., 2001. Determination of molybdenum isotope fractionation by double-spike multicollector inductively coupled plasma mass spectrometry. Geochem., Geophys. Geosys.2, Paper number 2000GC000124.

69. Slack, J. F., Cannon, W. F., 2009. Extraterrestrial demise of banded iron formations 1.85 billion years ago. Geology, 37, 1011–1014. doi:10.1130/G30259A.1

70. Taylor, S., McLennan, S., 1995. The geochemical evolution of the continental crust. Rev. Geophys. 2, 241–265.

71. Thomson, D., Rainbird, R.H., Planavsky, N.J., Lyons, T.W., Bekker, A., 2015. Chemostratigraphy of the Shaler Supergroup, Victoria Island, NW Canada: a record of ocean composition prior to the Cryogenian glaciations, Precamb. Res. 263, 232-245.

72. Tossell, J. A., 2005. Calculating the partitioning of the isotopes of Mo between oxidic and sulfidic species in aqueous solution. Geochim. Cosmochim. Acta, 69, 2981–2993. doi:10.1016/j.gca.2005.01.016

73. Zerkle, A.L., Poulton, S.W., Newton, R.J., Mettam, C., Claire, M.W., Bekker, A., Junium, C.K., 2017. Onset of the aerobic nitrogen cycle during the Great Oxidation Event, Nature 542, 465-467.

845

**Table 1. XRD data.**

| Core | Depth [m] | K-Feldspar (%) | Plagioclase (%) | Quartz (%) | Clay - chlorite (%) | Mica - muscovite (%) | Pyrite (%) | | | | |
|---|---|---|---|---|---|---|---|---|---|---|---|
| **Core C-175 of the ~2.06 Ga Upper Zaogena Formation (UZF-II) from Karelia, Russia** | | | | | | | | | | | |
| C-175 | 16.60 | 7 | 6 | 44 | n.d | 39 | 4 | | | | |
| C-175 | 86.90 | 18 | 6 | 57 | n.d | 17 | 2 | | | | |
| C-175 | 95.30 | 10 | 8 | 67 | n.d | 13 | 2 | | | | |
| C-175 | 96.90 | 21 | 7 | 57 | n.d | 12 | 3 | | | | |
| C-175 | 194.80 | 10 | 41 | 33 | n.d | 12 | 4 | | | | |
| C-175 | 204.30 | 19 | 28 | 37 | n.d | 13 | 3 | | | | |
| **Core C-5190 of the ~2.06 Ga Upper Zaogena Formation (UZF-I) from Karelia, Russia** | | | | | | | | | | | |
| C-5190 | 156.00 | 31 | 23 | 33 | 6 | 6 | 1 | | | | |
| C-5190 | 184.00 | 18 | 19 | 47 | 5 | 11 | <1 | | | | |
| C-5190 | 199.00 | 22 | 16 | 57 | n.d | 5 | <1 | | | | |

| Core | Depth [m] | Dolomite (%) | Plagioclase (%) | Forsterite (%) | Fluorapatite (%) | Quartz (%) | Clay - chlorite (%) | Mica - muscovite (%) | Pyrite (%) | Jarosite (%) | Gypsum (%) | Pyrophyllite (%) |
|---|---|---|---|---|---|---|---|---|---|---|---|---|
| **Core Strat 2 of the ~2.15 Ga Sengoma Argillite Formation (SAF) from Botswana** | | | | | | | | | | | | |
| Strat2 | 156.70 | n.d | 33 | <1 | n.d | 35 | 3 | 21 | 1 | 6 | n.d | n.d |
| Strat2 | 173.67 | n.d | 24 | n.d | 4 | 38 | 3 | 25 | 3 | n.d | 3 | n.d |

| | | | | | | | | | | | | |
|---|---|---|---|---|---|---|---|---|---|---|---|---|
| Strat2 | 181.25 | 1 | 23 | n.d | n.d | 41 | 4 | 25 | 4 | n.d | 2 | n.d |
| Strat2 | 186.57 | n.d | 13 | n.d | n.d | 43 | 3 | 28 | 2 | 4 | n.d | 7 |
| | | | | | | | | | | | | |
| **Core** | **Depth [m]** | **K-Feldspar (%)** | **Quartz (%)** | **Clay - chlorite (%)** | **Mica - muscovite (%)** | **Pyrophyllite (%)** | **Pyrite (%)** | **Rhomboclase (%)** | **Szomolnokite (%)** | | | |
| **Core EBA-2 of the ~2.32 Ga Timeball Hill Formation (THF) from South Africa** | | | | | | | | | | | | |
| EBA2 | 1328.90 | 2 | 25 | 2 | 63 | 8 | <1 | n.d | n.d | | | |
| EBA2 | 1338.07 | 1 | 41 | n.d | 10 | n.d | 10 | 32 | 6 | | | |
| EBA2 | 1338.13 | 1 | 74 | 3 | 18 | 1 | 3 | n.d | n.d | | | |
| EBA2 | 1338.17 | n.d | 47 | 4 | 23 | <1 | 12 | n.d | 13 | | | |
| EBA2 | 1338.20 | 1 | 60 | 3 | 16 | 1 | 9 | n.d | 10 | | | |
| EBA2 | 1339.00 | 1 | 11 | 2 | 78 | 7 | <1 | n.d | n.d | | | |
| EBA2 | 1343.00 | 1 | 50 | 5 | 37 | 5 | 2 | n.d | n.d | | | |
| EBA2 | 1346.20 | 2 | 11 | 1 | 54 | 24 | 4 | n.d | 4 | | | |

850

Table 2. Geochemical data. Molybdenum isotope data are reported relative to our internal standard (SPEX) and relative to the NIST 3134 standard +0.25‰ as suggested by Nägler and others (2014). The Fe speciation content of FeCarb, $Fe_{Ox}$, $Fe_{Py}$ and $Fe_{Mag}$ represent the extraction steps of Acetate, Dithionite, CrS and Oxalate respectively. DOP is calculated as DOP=$Fe_{py}/(Fe_{py}+Fe_{HCl})$].

| Core Name | Depth (m) | $\delta^{98}$Mo SPEX | $\delta^{98}$Mo NIST +0.25 | 2se | Mo (ppm) | Mo/ TOC | $Fe_{Carb}$ wt.% | $Fe_{Ox}$ wt. % | $Fe_{Py}$ wt. % | $Fe_{Mag}$ wt.% | $Fe_{HCl}$ wt.% | $Fe_{HR}$ wt.% | $Fe_{T}$ wt. % | $Fe_{HR}$ /$Fe_{T}$ | $Fe_{PY}$/ $Fe_{HR}$ | DOP | TOC wt.% | Al wt.% | [Mn] ppm | [Cu] ppm | [U] ppm | [V] ppm | [Zn] ppm |
|---|---|---|---|---|---|---|---|---|---|---|---|---|---|---|---|---|---|---|---|---|---|---|---|
| **Core C-175 of the ~2.06 Ga Upper Zaogena Formation (UZF-II) from Karelia, Russia** | | | | | | | | | | | | | | | | | | | | | | | |
| C-175 | 16.6 | 0.69 | **0.57** | 0.11 | 1.6 | 0.56 | 0.10 | 0.12 | 1.60 | 0.11 | 1.04 | 1.93 | 3.35 | 0.58 | 0.83 | 0.61 | 2.88 | 7.43 | 51 | 5 | 2.0 | 147 | 34 |
| C-175 | 33.7 | 0.90 | **0.78** | 0.12 | 15.0 | 1.88 | 0.05 | 0.24 | 4.17 | 0.06 | 0.57 | 4.51 | 5.00 | 0.90 | 0.92 | 0.88 | 7.97 | 4.76 | 36 | 67 | 5.3 | 289 | 109 |
| C-175 | 36.5 | 0.76 | **0.64** | 0.13 | 44.3 | 6.41 | 0.03 | 0.11 | 2.32 | 0.02 | 0.21 | 2.48 | 2.58 | 0.96 | 0.93 | 0.92 | 6.91 | 4.87 | 13 | 89 | 5.9 | 461 | 86 |
| C-175 | 38.4 | 0.62 | **0.50** | 0.11 | 26.0 | 3.28 | 0.05 | | 5.97 | 0.05 | 0.00 | 6.06 | 5.83 | 1.00 | 0.98 | 1.00 | 7.94 | 6.47 | 11 | 42 | 12.1 | 414 | 147 |
| C-175 | 54.9 | 0.79 | **0.67** | 0.10 | 180.2 | 10.77 | 0.17 | 0.03 | 7.49 | 0.04 | 1.73 | 7.73 | 7.94 | 0.97 | 0.97 | 0.81 | 16.73 | 4.06 | 43 | 321 | 35.7 | 957 | 484 |
| C-175 | 57.3 | 1.23 | **1.11** | 0.10 | 43.7 | 3.08 | 0.14 | 0.01 | 6.44 | 0.01 | 0.30 | 6.61 | 6.44 | 1.00 | 0.98 | 0.96 | 14.20 | 3.71 | 258 | 169 | 18.5 | 414 | 311 |
| C-175 | 61.5 | 0.44 | **0.32** | 0.12 | 35.2 | 5.34 | 0.00 | 0.00 | 1.65 | 0.00 | 0.00 | 1.66 | 3.33 | 0.50 | 1.00 | 1.00 | 6.59 | 1.20 | 35 | 22 | 7.8 | 353 | 63 |
| C-175 | 70.6 | 1.95 | **1.83** | 0.11 | 18.0 | 3.33 | 0.16 | 0.01 | 0.51 | 0.00 | 0.47 | 0.69 | 2.58 | 0.27 | 0.74 | 0.52 | 5.40 | 2.77 | 25 | 86 | 4.9 | 269 | 63 |
| C-175 | 72.6 | 0.84 | **0.72** | 0.12 | 13.4 | 1.41 | 0.00 | 0.02 | 1.59 | 0.00 | 0.04 | 1.61 | 1.55 | 1.00 | 0.99 | 0.98 | 9.52 | 4.13 | 28 | 187 | 7.3 | 399 | 224 |
| C-175 | 75.2 | 0.80 | **0.68** | 0.09 | 5.7 | 0.86 | 0.00 | 0.01 | 0.92 | 0.00 | 0.02 | 0.94 | 1.05 | 0.89 | 0.98 | 0.98 | 6.61 | 2.54 | 23 | 83 | 1.7 | 123 | 124 |
| C-175 | 80.3 | 0.89 | **0.77** | 0.10 | 7.4 | 0.60 | 0.00 | 0.01 | 0.83 | 0.00 | 0.00 | 0.84 | 0.87 | 0.96 | 0.99 | 1.00 | 12.43 | 2.96 | 24 | 118 | 3.3 | 193 | 95 |
| C-175 | 86.9 | 0.70 | **0.58** | 0.09 | 40.2 | 1.89 | 0.02 | 0.12 | 0.78 | 0.00 | 0.07 | 0.93 | 1.38 | 0.67 | 0.84 | 0.92 | 21.27 | 3.61 | 24 | 400 | 10.7 | 587 | 486 |
| C-175 | 95.3 | 0.50 | **0.38** | 0.12 | 107.3 | 4.83 | 0.05 | 0.04 | 0.88 | 0.01 | 0.18 | 0.98 | 1.07 | 0.91 | 0.90 | 0.83 | 22.22 | 2.50 | 15 | | 14.9 | 864 | |
| C-175 | 96.9 | 0.87 | **0.75** | 0.13 | 41.8 | 1.51 | 0.04 | 0.02 | 1.56 | 0.01 | 0.00 | 1.62 | 1.57 | 1.03 | 0.96 | 1.00 | 27.77 | 3.40 | 19 | 572 | 13.9 | 687 | 265 |
| C-175 | 97.0 | 0.93 | **0.81** | 0.13 | 15.1 | 0.89 | 0.02 | 0.01 | 2.12 | 0.00 | 0.00 | 2.16 | 2.47 | 0.87 | 0.98 | 1.00 | 16.96 | 3.81 | 56 | 119 | 4.7 | 256 | 558 |
| C-175 | 98.8 | 1.05 | **0.93** | 0.13 | 3.2 | 0.20 | 0.01 | 0.07 | 1.22 | 0.02 | 0.05 | 1.32 | 1.27 | 1.00 | 0.92 | 0.96 | 16.30 | 4.26 | 30 | 70 | 3.6 | 196 | 208 |

| | | | | | | | | | | | | | | | | | | | | | | | |
|---|---|---|---|---|---|---|---|---|---|---|---|---|---|---|---|---|---|---|---|---|---|---|---|
| C-175 | 101.5 | 0.90 | **0.78** | 0.12 | 2.1 | 0.12 | 0.03 | 0.02 | 1.13 | 0.02 | 0.33 | 1.20 | 1.35 | 0.89 | 0.94 | 0.77 | 17.14 | 4.00 | 29 | 48 | 3.1 | 222 | 55 |
| C-175 | 175.2 | 0.66 | **0.54** | 0.12 | 13.6 | 1.32 | 0.52 | 0.24 | 1.61 | 0.01 | 4.12 | 2.38 | 4.63 | 0.51 | 0.68 | 0.28 | 10.32 | 4.91 | 401 | 63 | 4.5 | 309 | 145 |
| C-175 | 176.0 | 0.79 | **0.67** | 0.08 | 17.7 | 1.79 | 0.43 | 0.27 | 1.59 | 0.01 | 3.33 | 2.30 | 3.39 | 0.68 | 0.69 | 0.32 | 9.90 | 3.93 | 173 | 35 | 4.5 | 152 | 287 |
| C-175 | 179.4 | 0.75 | **0.63** | 0.10 | 6.4 | 0.80 | 0.54 | 0.33 | 1.91 | 0.01 | 2.77 | 2.80 | 3.99 | 0.70 | 0.68 | 0.41 | 8.02 | 5.36 | 273 | 6 | 2.3 | 212 | 91 |
| C-175 | 180.7 | 0.88 | **0.76** | 0.11 | 4.3 | 0.91 | 0.54 | 0.41 | 2.36 | 0.02 | 3.03 | 3.33 | 5.03 | 0.66 | 0.71 | 0.44 | 4.73 | 6.94 | 251 | 67 | 1.8 | 288 | 124 |
| C-175 | 194.8 | 1.23 | **1.11** | 0.09 | 6.5 | 3.96 | 0.30 | 0.03 | 1.66 | 0.05 | 1.03 | 2.03 | 3.25 | 0.63 | 0.82 | 0.62 | 1.64 | 7.62 | 116 | 18 | 3.4 | 467 | 76 |
| C-175 | 204.3 | 0.66 | **0.54** | 0.12 | 6.8 | 0.79 | 0.03 | 0.02 | 1.71 | 0.03 | 0.60 | 1.79 | 2.98 | 0.60 | 0.95 | 0.74 | 8.56 | 6.48 | 68 | 171 | 4.1 | 250 | 240 |
| **Core C-5190 of the ~2.06 Ga Upper Zaogena Formation (UZF-I) from Karelia, Russia** | | | | | | | | | | | | | | | | | | | | | | | |
| C-5190 | 16.0 | 0.58 | **0.46** | 0.09 | 35.2 | 1.93 | 0.01 | 0.08 | 0.09 | 0.16 | 1.49 | 0.34 | 2.04 | 0.17 | 0.27 | 0.06 | 18.28 | 4.87 | 100 | 219 | 5.3 | 586 | 522 |
| C-5190 | 78.0 | 0.84 | **0.72** | 0.05 | 24.2 | 3.02 | 0.17 | 0.02 | 0.08 | 0.02 | 0.73 | 0.29 | 3.04 | 0.10 | 0.28 | 0.10 | | 5.93 | 508 | 23 | 2.8 | 276 | 78 |
| C-5190 | 83.0 | 1.13 | **1.01** | 0.05 | 13.2 | 1.41 | 0.16 | 0.70 | 1.31 | 0.38 | 2.21 | 2.55 | 3.78 | 0.70 | 0.51 | 0.50 | 9.34 | 5.01 | 365 | 26 | 2.1 | 199 | 221 |
| C-5190 | 96.0 | 0.35 | **0.23** | 0.10 | 27.2 | 1.76 | 0.12 | 0.29 | 0.48 | 0.30 | 1.60 | 1.19 | 3.49 | 0.34 | 0.40 | 0.23 | 15.48 | 4.69 | 367 | 48 | 5.7 | 424 | 207 |
| C-5190 | 100.0 | 0.47 | **0.35** | 0.10 | 14.5 | 0.68 | 0.05 | 0.25 | 0.46 | 0.25 | 1.19 | 1.00 | 2.32 | 0.43 | 0.46 | 0.28 | 21.34 | 3.21 | 216 | 4 | 4.1 | 269 | 430 |
| C-5190 | 137.0 | 0.28 | **0.16** | 0.05 | 13.9 | 2.11 | 0.26 | 0.18 | 0.09 | 0.77 | 5.28 | 1.30 | 6.28 | 0.22 | 0.07 | 0.02 | 6.59 | 6.28 | 377 | 60 | 2.0 | 524 | 77 |
| C-5190 | 156.0 | 1.06 | **0.94** | 0.08 | 13.2 | 1.17 | 0.09 | 0.10 | 0.72 | 0.15 | | 1.07 | 3.03 | 0.35 | 0.67 | | 11.30 | 6.35 | 64 | 35 | 3.8 | 211 | 29 |
| C-5190 | 184.0 | 1.04 | **0.92** | 0.11 | 70.7 | 2.82 | 0.02 | 0.07 | 0.12 | 0.09 | 0.62 | 0.29 | 1.19 | 0.24 | 0.41 | 0.16 | 25.11 | 4.93 | 66 | 298 | 9.0 | | |
| C-5190 | 199.0 | 0.71 | **0.59** | 0.05 | 27.4 | 1.10 | 0.03 | 0.02 | 0.19 | 0.08 | 0.26 | 0.33 | 0.58 | 0.58 | 0.59 | 0.42 | 25.00 | 2.39 | 39 | 91 | 4.6 | 160 | 672 |
| C-5190 | 245.0 | 1.32 | **1.20** | 0.11 | 8.2 | 0.50 | 0.20 | 0.21 | 0.72 | 0.38 | | 1.50 | 3.72 | 0.40 | 0.48 | | 16.48 | 3.81 | 267 | 85 | 4.5 | 229 | 21 |
| C-5190 | 292.5 | 1.57 | **1.45** | 0.11 | 2.0 | 0.19 | 0.36 | 0.19 | 0.38 | 0.36 | 2.55 | 1.30 | 4.42 | 0.29 | 0.29 | 0.13 | 10.40 | 4.71 | 537 | 52 | 0.8 | 189 | 51 |
| C-5190 | 293.2 | 1.53 | **1.41** | 0.13 | 1.7 | 0.20 | 0.03 | 0.07 | 0.24 | 0.09 | 0.40 | 0.43 | 0.66 | 0.66 | 0.55 | 0.38 | 8.50 | 1.29 | 156 | 17 | 0.5 | 26 | 4 |
| C-5190 | 295.6 | 1.29 | **1.17** | 0.10 | 1.7 | 0.61 | 0.55 | 0.42 | 0.26 | 0.68 | 3.82 | 1.91 | 9.70 | 0.20 | 0.14 | 0.06 | 2.78 | 8.37 | | 13 | 0.5 | 315 | 105 |

| | | | | | | | | | | | | | | | | | | | | | | | |
|---|---|---|---|---|---|---|---|---|---|---|---|---|---|---|---|---|---|---|---|---|---|---|---|
| **Core Strat 2 of the ~2.15 Ga Sengoma Argillite Formation (SAF) from Botswana** | | | | | | | | | | | | | | | | | | | | | | | |
| Strat2 | 142.8 | 0.36 | **0.24** | 0.05 | 2.6 | 0.29 | 0.00 | 0.25 | 0.50 | 0.71 | 2.21 | 0.43 | 3.35 | 0.43 | 0.34 | 0.18 | 9.20 | 8.44 | 359 | 35 | 2.6 | 124 | 94 |
| Strat2 | 156.8 | 2.33 | **2.21** | 0.06 | 1.9 | 0.27 | 0.10 | 1.23 | 0.76 | 0.30 | 2.36 | 0.84 | 2.85 | 0.84 | 0.32 | 0.24 | 7.10 | 7.06 | 251 | 52 | 2.7 | 134 | 69 |
| Strat2 | 171.5 | 1.25 | **1.13** | 0.05 | 1.9 | 0.19 | 0.10 | 0.14 | 2.01 | 0.17 | 0.62 | 0.90 | 2.68 | 0.90 | 0.83 | 0.76 | 10.00 | 5.91 | 291 | 31 | 3.0 | 113 | 99 |
| Strat2 | 173.7 | 1.25 | **1.13** | 0.04 | 2.2 | 0.51 | 0.06 | 0.29 | 2.50 | 0.02 | 0.49 | 0.93 | 3.08 | 0.93 | 0.87 | 0.84 | 4.20 | 7.05 | 50 | 38 | 2.2 | 101 | 44 |
| Strat2 | 177.7 | 1.31 | **1.19** | 0.06 | 2.0 | 0.22 | 0.13 | 0.08 | 1.90 | 0.17 | 0.47 | 0.86 | 2.66 | 0.86 | 0.83 | 0.80 | 8.90 | 5.00 | 427 | 34 | 2.8 | 128 | 53 |
| Strat2 | 181.3 | 1.64 | **1.52** | 0.05 | 2.1 | 0.27 | 0.07 | 0.16 | 3.02 | 0.03 | 0.32 | 0.91 | 3.60 | 0.91 | 0.92 | 0.90 | 7.80 | 6.91 | 158 | 44 | 3.0 | 138 | 106 |
| Strat2 | 186.6 | 0.82 | **0.70** | 0.05 | 36.6 | 3.33 | 0.24 | 0.70 | 2.44 | 0.07 | 1.59 | 0.93 | 3.72 | 1.00 | 0.75 | 0.61 | 11.00 | 6.72 | 91 | 55 | 26.0 | | 86 |
| Strat2 | 200.7 | 1.61 | **1.49** | 0.04 | 10.9 | 0.76 | 0.11 | 0.11 | 2.82 | 0.03 | 0.34 | 3.04 | 3.49 | 0.87 | 0.93 | 0.89 | 14.40 | 4.65 | 318 | 54 | 3.3 | 231 | 84 |
| Strat2 | 202.5 | 1.72 | **1.60** | 0.05 | 6.6 | 0.43 | 0.10 | 0.09 | 2.73 | 0.06 | 0.45 | 0.92 | 3.24 | 0.92 | 0.92 | 0.86 | 15.30 | 3.45 | 319 | 46 | 4.8 | 198 | 76 |
| Strat2 | 205.3 | 1.82 | **1.70** | 0.04 | 8.7 | 0.58 | 0.10 | 0.12 | 2.93 | 0.02 | 0.46 | 1.00 | 3.15 | 1.00 | 0.92 | 0.86 | 14.20 | 4.55 | 198 | 48 | 4.6 | 182 | 72 |
| Strat2 | 209.0 | 1.63 | **1.51** | 0.04 | 8.8 | 0.53 | 0.10 | 0.16 | 2.01 | 0.06 | 0.59 | 0.77 | 3.04 | 0.77 | 0.86 | 0.77 | 16.60 | 6.10 | 265 | 57 | 4.1 | 214 | 112 |
| Strat2 | 212.7 | 0.94 | **0.82** | 0.04 | 4.8 | 0.34 | 0.20 | 0.09 | 2.10 | 0.08 | 0.39 | 0.91 | 2.71 | 0.91 | 0.85 | 0.84 | 14.10 | 4.60 | 353 | 34 | 3.2 | 148 | 60 |
| Strat2 | 216.8 | 0.83 | **0.71** | 0.06 | 1.4 | 0.13 | 0.10 | 0.14 | 1.82 | 0.34 | 0.71 | 1.04 | 2.30 | 1.00 | 0.76 | 0.72 | 10.70 | 4.41 | 378 | 34 | 2.6 | 133 | 81 |
| Strat2 | 238.0 | 0.12 | **0.00** | 0.06 | 1.5 | 0.21 | 0.11 | 0.05 | 0.07 | 0.31 | 0.00 | 0.12 | 4.48 | 0.12 | 0.13 | | 7.04 | 8.41 | 147 | 3 | 3.8 | 151 | 55 |
| Strat2 | 286.6 | 1.37 | **1.25** | 0.04 | 2.0 | 0.13 | 0.10 | 0.00 | 0.60 | 0.20 | 1.16 | 0.25 | 3.59 | 0.25 | 0.67 | 0.34 | 15.30 | 4.87 | 728 | 31 | 1.7 | 144 | 67 |
| **Core EBA-2 of the ~2.32 Ga Timeball Hill Formation (THF) from South Africa** | | | | | | | | | | | | | | | | | | | | | | | |
| EBA2 | 1327.7 | 0.15 | **0.03** | 0.14 | 8.9 | 2.47 | 0.24 | 0.35 | 1.16 | 0.49 | 7.76 | 2.24 | 7.31 | 0.31 | 0.52 | 0.13 | 3.59 | 9.87 | 285 | 155 | 12.4 | 107 | 1024 |
| EBA2 | 1327.8 | -0.25 | **-0.37** | 0.12 | 21.5 | 7.85 | 0.00 | 0.14 | 0.93 | 0.73 | 1.64 | 1.80 | 4.61 | 0.39 | 0.52 | 0.36 | 2.74 | 11.34 | 57 | 79 | 8.1 | 83 | 431 |
| EBA2 | 1327.9 | 0.57 | **0.45** | 0.14 | 7.6 | 2.22 | 0.48 | 0.08 | 0.70 | 0.17 | 5.13 | 1.43 | 5.77 | 0.25 | 0.49 | 0.12 | 3.45 | 10.86 | 265 | 302 | 10.0 | 99 | 616 |
| EBA2 | 1328.9 | -0.01 | **-0.13** | 0.12 | 6.9 | 1.61 | 0.51 | 0.07 | 1.00 | 2.54 | 2.45 | 4.12 | 4.74 | 0.87 | 0.24 | 0.29 | 4.30 | 11.35 | 70 | 102 | 11.2 | 119 | 347 |

| | | | | | | | | | | | | | | | | | | | | | | | |
|---|---|---|---|---|---|---|---|---|---|---|---|---|---|---|---|---|---|---|---|---|---|---|---|
| EBA2 | 1338.1 | 0.04 | **-0.08** | 0.04 | 67.7 | 47.31 | 0.99 | 0.15 | 6.59 | 0.02 | 2.44 | 7.80 | 18.37 | 0.42 | 0.85 | 0.73 | 1.43 | 1.87 | 465 | 71 | 24.7 | 63 | 39 |
| EBA2 | 1338.1 | 0.10 | **-0.02** | 0.04 | 14.9 | 4.96 | 0.29 | 0.06 | 2.01 | 0.02 | 1.12 | 2.43 | 2.72 | 0.89 | 0.85 | 0.64 | 3.01 | 4.88 | 155 | 38 | 20.6 | 163 | 783 |
| EBA2 | 1338.2 | 1.37 | **1.25** | 0.04 | 54.6 | 20.21 | 0.49 | 0.08 | 6.68 | 0.04 | 2.58 | 7.44 | 13.42 | 0.55 | 0.92 | 0.72 | 2.70 | 5.02 | 232 | 227 | 17.6 | 185 | |
| EBA2 | 1338.2 | 0.48 | **0.36** | 0.04 | 20.9 | 10.93 | 0.66 | 0.09 | 9.03 | 0.03 | 1.97 | 10.04 | 10.69 | 0.94 | 0.92 | 0.82 | 1.91 | 4.37 | 387 | 146 | 39.6 | 175 | |
| EBA2 | 1339.0 | -0.22 | **-0.34** | 0.06 | 4.3 | 10.58 | 0.04 | 0.02 | 0.14 | 0.00 | 0.24 | 0.20 | 0.46 | 0.43 | 0.71 | 0.36 | 0.41 | 15.74 | 77 | 256 | 12.6 | 173 | 116 |
| EBA2 | 1343.0 | 0.83 | **0.71** | 0.04 | 4.4 | 12.88 | 0.18 | 0.04 | 2.60 | 0.11 | 1.40 | 2.93 | 5.50 | 0.53 | 0.89 | 0.65 | 0.34 | 8.57 | 232 | 29 | 5.5 | 123 | 64 |
| EBA2 | 1346.2 | -0.26 | **-0.38** | 0.04 | 5.5 | 16.15 | 0.13 | 0.04 | 0.77 | 0.01 | 1.24 | 0.94 | 5.46 | 0.17 | 0.82 | 0.38 | 0.34 | 12.21 | 77 | 150 | 5.6 | 227 | 52 |

851

852

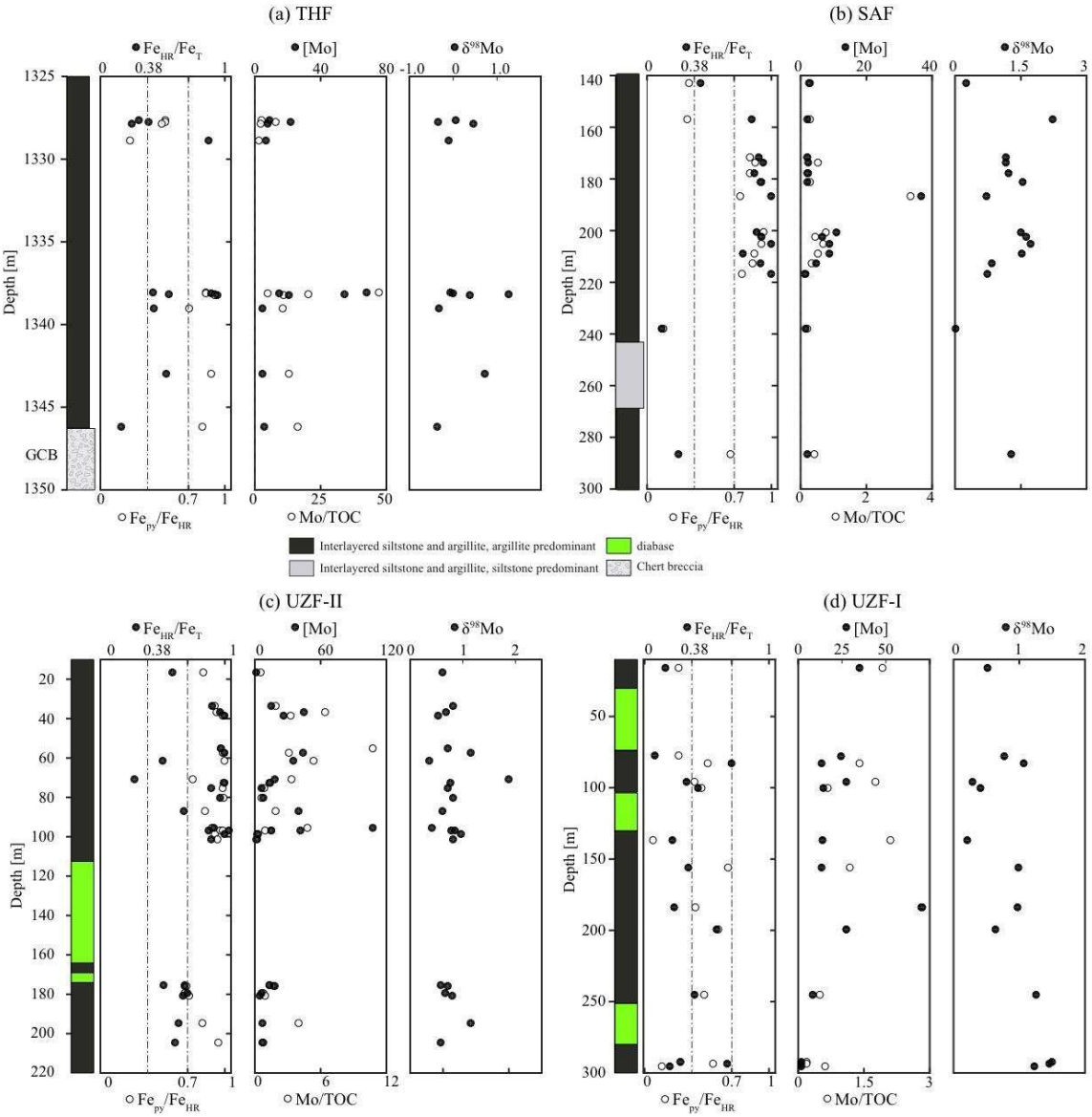


853

854

855

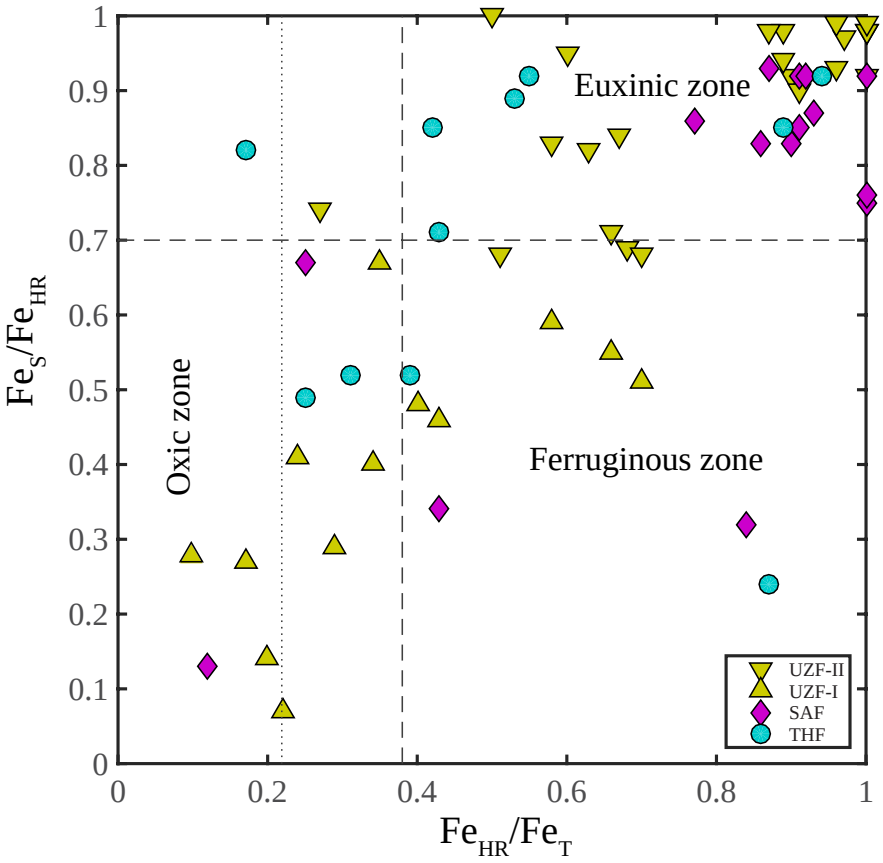
Euxinic zone
Oxic zone
Ferruginous zone
UZF-II
UZF-I
SAF
THF
$Fe_S/Fe_{HR}$
$Fe_{HR}/Fe_T$
0
0.1
0.2
0.3
0.4
0.5
0.6
0.7
0.8
0.9
1
0
0.2
0.4
0.6
0.8
1

856

857

858

859

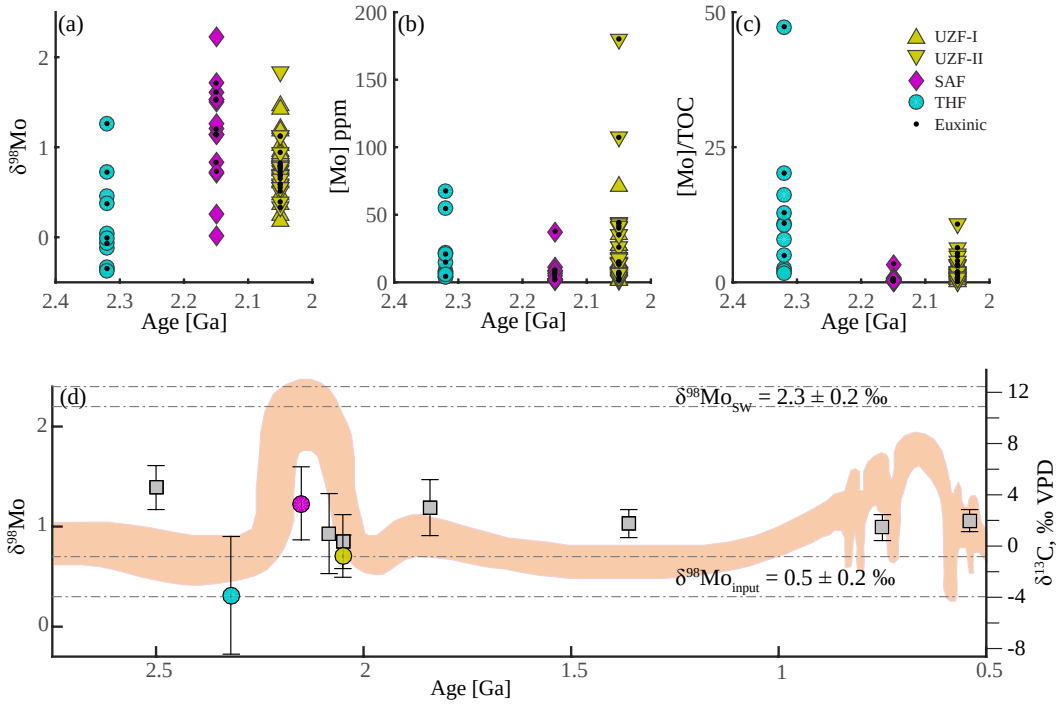


860

861

862

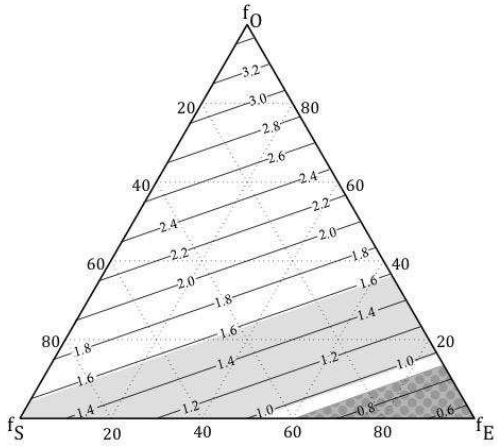


a) $\delta^{98}Mo_{SW}$ in flux space

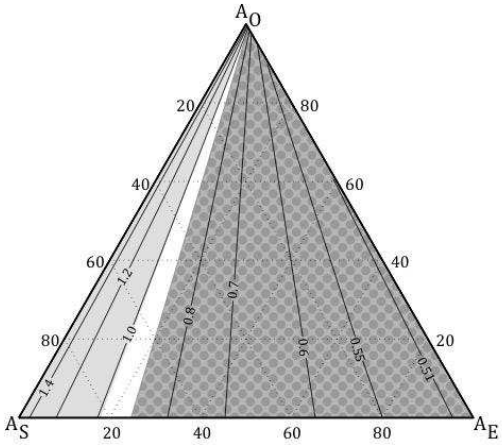


b) $\delta^{98}Mo_{SW}$ in area space

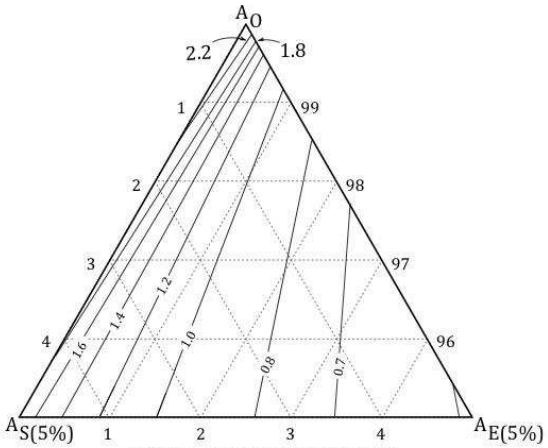


c) $\delta^{98}Mo_{SW}$ in area space, upper 5%

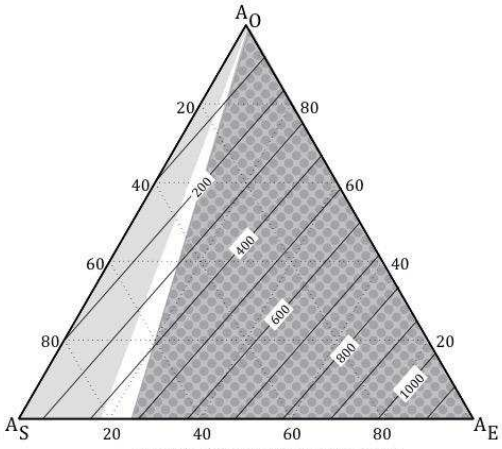


d) global burial rate in area space

863

864

865

866

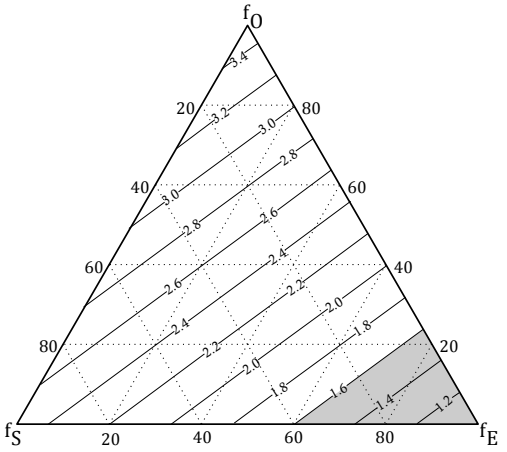


a) $\delta^{98}Mo_{sw}$ in flux space

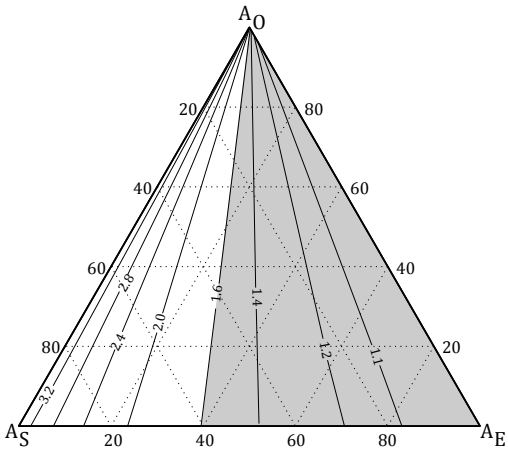


b) $\delta^{98}Mo_{sw}$ in area space

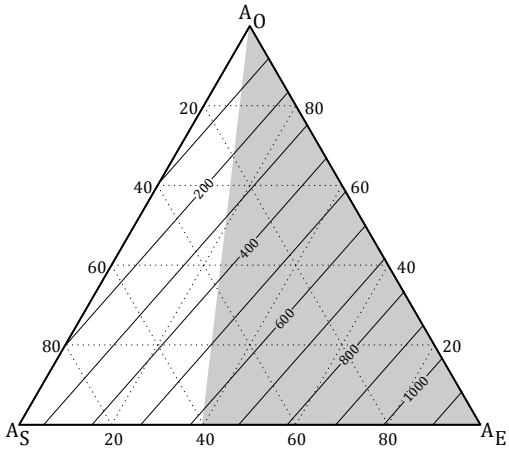


c) global burial rate in area space

867

868

869

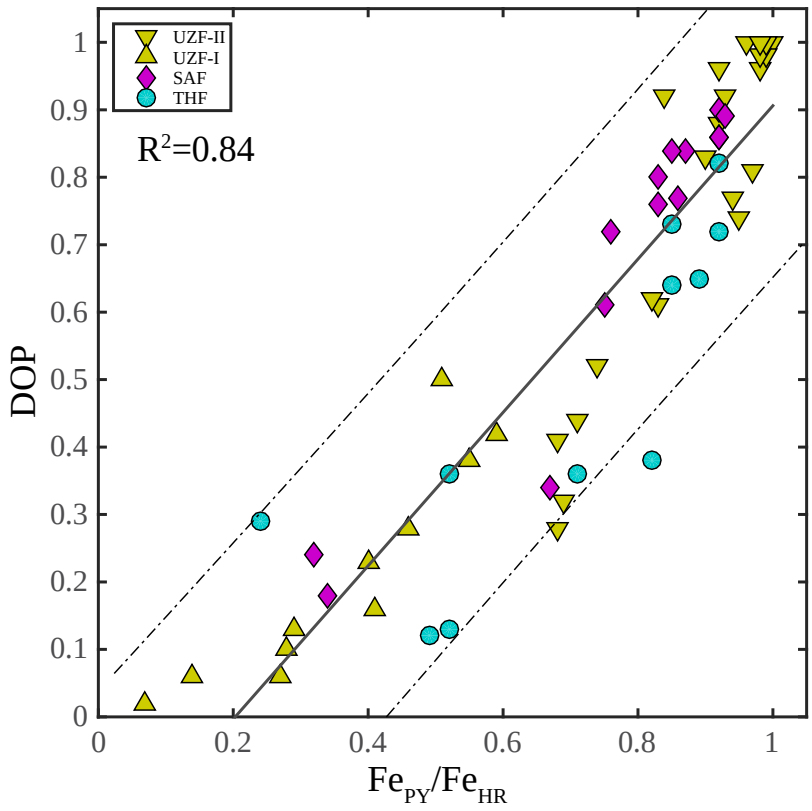


870

871

872

873

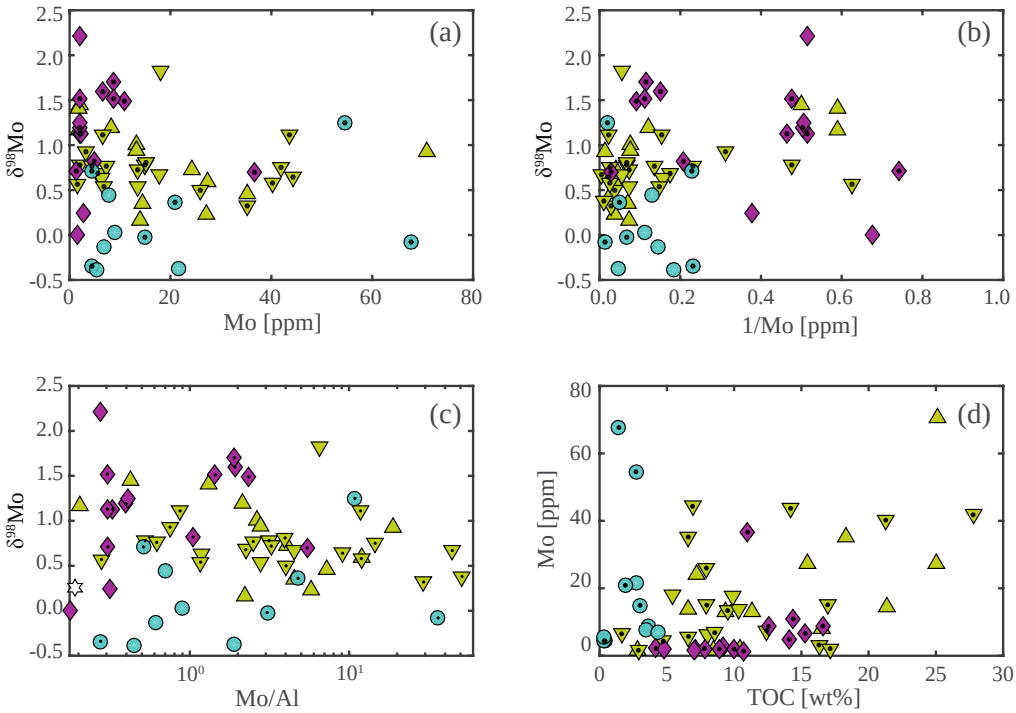


874

875

876

877

878